The Astrophysical Journal, 988:162 (23pp), 2025 August 1 https://doi.org/10.3847/1538-4357/addf4c

Constraining Resolved Extragalactic R_{21} Variation with Well-calibrated ALMA Observations

Jakob den Brok[1], Elias K. Oakes[2], Adam K. Leroy[3,4], Eric W. Koch[1], Antonio Usero[5], Erik W. Rosolowsky[6], Frank Bigiel[7], Jiayi Sun (孙嘉懿)[8,14], Hao He[7], Ashley T. Barnes[9], Yixian Cao[10], Fu-Heng Liang[9,11], Hsi-An Pan[12], Toshiki Saito[13], Sumit K. Sarbadhicary[3,4], and Thomas G. Williams[11]
[1] Center for Astrophysics | Harvard Smithsonian, 60 Garden Street, Cambridge, MA 02138, USA; jakob.denbrok@gmail.com
[2] Department of Physics, University of Connecticut, 196A Auditorium Road, Storrs, CT 06269, USA
[3] Department of Astronomy, The Ohio State University, 140 West 18th Avenue, Columbus, OH 43210, USA
[4] Center for Cosmology and Astroparticle Physics (CCAPP), 191 West Woodruff Avenue, Columbus, OH 43210, USA
[5] Observatorio Astronómico Nacional (IGN), C/Alfonso XII, 3, E-28014 Madrid, Spain
[6] Department of Physics, University of Alberta, Edmonton, AB T6G 2E1, Canada
[7] Argelander-Institut für Astronomie, Universität Bonn, Auf dem Hügel 71, 53121 Bonn, Germany
[8] Department of Astrophysical Sciences, Princeton University, 4 Ivy Lane, Princeton, NJ 08544, USA
[9] European Southern Observatory, Karl-Schwarzschild Straße 2, D-85748 Garching bei München, Germany
[10] Max-Planck-Institut für extraterrestrische Physik, Giessenbachstraße 1, D-85748 Garching, Germany
[11] Sub-department of Astrophysics, Department of Physics, University of Oxford, Keble Road, Oxford OX1 3RH, UK
[12] Department of Physics, Tamkang University, No.151, Yingzhuan Road, Tamsui Dist., New Taipei City 251301, Taiwan
[13] National Astronomical Observatory of Japan, 2-21-1 Osawa, Mitaka, Tokyo, 181-8588, Japan
Received 2024 September 20; revised 2025 May 26; accepted 2025 May 30; published 2025 July 22

Abstract

CO(1–0) and CO(2–1) are commonly used as bulk molecular gas tracers. The CO line ratios (especially CO(2–1)/CO(1–0)–R_{21}) vary within and among galaxies, yet previous studies on R_{21} and alike often rely on measurements constructed by combining data from facilities with substantial relative calibration uncertainties that have the same order as physical line ratio variations. Hence, robustly determining systematic R_{21} variations is challenging. Here, we compare CO(1–0) and CO(2–1) mapping data from ALMA for 14 nearby galaxies, at a common physical resolution of 1.7 kpc. Our data set includes new ALMA (7 m+TP) CO(1–0) maps of 12 galaxies. We investigate R_{21} variation to understand its dependence on global galaxy properties, kiloparsec-scale environmental factors, and its correlation with star formation rate (SFR) surface density and metallicity. We find that the galaxy-to-galaxy scatter is 0.05 dex. This is lower than previous studies, which reported over 0.1 dex variation, likely reflecting significant flux calibration uncertainties in single-dish surveys. Within individual galaxies, R_{21} has a typical mean value of ∼0.64 and 0.1 dex variation, with an increase to ∼0.75 toward galactic centers. We find strong correlations between R_{21} and various galactic parameters, particularly SFR surface density, which shows a power-law slope of 0.10–0.11 depending on the adopted binning/fitting methods. Our findings suggest that, for studies covering main-sequence galaxy samples, assuming a fixed $R_{21} = 0.64$ does not significantly bias kiloparsec-scale molecular gas mass estimates from CO(2–1). Instead, systematic uncertainties from flux calibration and the CO-to-H_2 conversion factor account for more systematic scatter of CO-derived molecular gas properties.

Unified Astronomy Thesaurus concepts: Interstellar medium (847); Spiral galaxies (1560); Molecular gas (1073); Millimeter-wave spectroscopy (2252); Radio interferometry (1346)

1. Introduction

The lowest rotational-J transitions of carbon monoxide ($^{12}C^{16}O$, hereafter CO) constitute an accessible way to trace the bulk distribution and kinematics of the molecular gas across galaxies (P. M. Solomon et al. 1987; J. S. Young & N. Z. Scoville 1991; A. D. Bolatto et al. 2013). In contrast to the most abundant molecule, H_2, the CO molecule has a permanent dipole moment and the ground transition $J = 1 \rightarrow 0$ is excited at ∼5.5 K, allowing CO emission to trace gas at the cold temperatures typical of most H_2 in galaxies necessary for star formation to occur. The mass distribution of the molecular gas is then determined using a CO-to-H_2 conversion factor, which is expected to be depend on local environment extragalactic environment (R. L. Dickman et al. 1986; J. S. Young & N. Z. Scoville 1991; P. M. Bryant & N. Z. Scoville 1996; A. D. Bolatto et al. 2013).

Furthermore, the critical density of the low rotational-J CO transitions is relatively modest with $n_{\mathrm{crit},1-0} \approx 570\,\mathrm{cm}^{-3}$ and $n_{\mathrm{crit},2-1} \approx 4400\,\mathrm{cm}^{-3}$, respectively, for the optical thin case at $T_{\mathrm{kin}} = 20\,K$ (see Table 4 in E. Schinnerer & A. K. Leroy 2024). For optically thick emission, the critical densities are further reduced by radiative trapping. For typical optical depths of $\tau \sim 5$, the effective critical densities are $n_{\mathrm{crit},1-0} \approx 100\,\mathrm{cm}^{-3}$ and $n_{\mathrm{crit},2-1} \approx 500\,\mathrm{cm}^{-3}$ (consistent with the effective excitation density estimates from Y. L. Shirley 2015). Most CO emission in galaxies is optically thick, and these effective critical densities align well with the typical mean densities of molecular gas in the interstellar medium (ISM; A. D. Bolatto et al. 2013; M. Heyer & T. M. Dame 2015). As a result, both CO(1–0) and (2–1) are effective tracers of the bulk of the molecular gas in galaxies. Practically, the low rotation-J CO

[14] NASA Hubble Fellow.

lines are also almost always the lines that show the highest brightness temperatures in the ground-accessible $\lambda \sim 1$–3 mm wavelengths. In contrast, higher-J CO lines (almost always) require longer integration times to be detected and probe a smaller fraction of gas, which is typically warmer and denser than the average, more widely distributed, colder and less dense H_2 gas phase. Given these factors, the lowest rotational-J transitions represent our best tools to observe the molecular gas with ground-based telescopes.

While theoretical work on interpreting and using CO as a H_2 tracer often focuses on the CO(1–0) transition (e.g., L. Bassini et al. 2020; L. C. Keating et al. 2020; D. Seifried et al. 2020; C.-Y. Hu et al. 2023; though see M. Gong et al. 2020; C. H. Peñaloza et al. 2017), observations of galaxies in the local Universe ($z < 0.1$) have started to target the $J = 2 \rightarrow 1$ transition instead of the $J = 1 \rightarrow 0$ ground transition (e.g., A. K. Leroy et al. 2009, 2021b; T. Brown et al. 2021; V. Villanueva et al. 2024). There are several reasons that make current observation of CO(2–1) advantageous over CO(1–0): (i) Because CO(2–1) lies at a higher frequency (230.5 GHz instead of 115.3 GHz), it can be observed at a higher angular resolution by a given single-dish telescope or fixed configuration array; (ii) the CO(1–0) emission line lies 2.7 GHz from the strong O_2 telluric absorption feature at 118 GHz. Therefore, under dry atmospheric conditions present at sites such as the Atacama desert, the CO(2–1) emission is slightly less attenuated than the CO(1–0) emission line for targets in the Milky Way or in the nearby Universe (i.e., for small or negligible redshifts of $z < 0.1$ as for higher z, the line will shift out of the telluric absorption feature); (iii) when considering the capabilities of the astronomical interferometer at the Atacama Large Millimeter/submillimeter Array (ALMA), given (i) and (ii), for a fixed target angular resolution the CO(2–1) emission line can generally be mapped 2–4 times faster than CO(1–0) for the same sensitivity and angular resolution;[15] (iv) CO(2–1) is accessible over a broader redshift range for millimeter interferometers, enabling studies of molecular gas across a wider range of cosmic time. Given these points, combining high luminosity with the ability to trace the bulk of the H_2 mass in GMCs makes the CO(2–1) line an important tracer of molecular gas that needs to calibrated for use across diverse environments.

Given the sensitivity of the CO line intensity to changes in the underlying molecular gas conditions, obtaining accurate measurements of the line ratio R_{21} is crucial for interpreting CO(2–1) observations and translating them into meaningful insights about the molecular gas. The measured line ratio will depend on the ISM physical conditions. In the case of extragalactic observations with large, often ∼kpc, beams, an individual measurement will combine an ensemble of GMCs with potentially distinct physical properties (such as size, mass, or average temperature). From theoretical work on a local, GMC-scale level, we expect the CO emission of different rotational transitions (and hence the resulting CO line ratio R_{21}, yet more weakly) to depend to various degrees on the GMC-averaged kinetic gas temperature, $T_{\rm kin}$, the collider density, $n_{\rm H_2}$, the column density of CO, $N_{\rm CO}$, and the CO line velocity dispersion Δv (A. D. Bolatto et al. 2013; A. K. Leroy et al. 2017; C. H. Peñaloza et al. 2017; M. Gong et al. 2020). As these local quantities vary as a function of environment within galaxies, we therefore expect systematic variation of R_{21}.

R_{21} has been measured and its variations studied in the Milky Way (e.g., S. Sakamoto et al. 1994; T. Hasegawa et al. 1997; T. Sawada et al. 2001) and nearby galaxies (e.g., A. Eckart et al. 1990; J. Braine & F. Combes 1992; J. Braine et al. 1993; P. P. Papadopoulos & E. R. Seaquist 1998; Y. Yajima et al. 2021; R. P. Keenan et al. 2025). For instance, studying the Orion A and B clouds in the Milky Way, S. Sakamoto et al. (1994) found an average value of ∼0.66–0.77, with values above unity found for the molecular gas near active SF sites, where photodissociation regions and H II regions are located. Moreover, previous studies have reported a correlation of the ratio R_{21} with the molecular gas density, as R_{21} decreases with lower gas densities from the centers to the edges of Milky Way molecular clouds (T. Hasegawa et al. 1997; T. Yoda et al. 2010). In addition, in other galaxies, radial trends have been reported with higher average values toward galactic centers (J. Braine & F. Combes 1992; A. K. Leroy et al. 2009). Promising tracers of R_{21} variation include the star formation rate (SFR) surface density, or the molecular gas depletion time (D. Narayanan & M. R. Krumholz 2014; I. Lamperti et al. 2020; J. S. den Brok et al. 2021; Y. Yajima et al. 2021; A. K. Leroy et al. 2022; R. P. Keenan et al. 2025). However, constraining the variation and obtaining such proxies of the line ratio is not just a technical detail, but a critical step to enable quantitative use of CO(2–1) emission to infer molecular gas masses in nearby galaxies. This, in turn, is key to maximize the scientific return of modern millimeter-wave observatories.

Extragalactic mapping of CO line ratios has mainly been confined to single- or a few galaxy studies (L. P. Crosthwaite & J. L. Turner 2007; J. Koda et al. 2012, 2020; C. J. Law et al. 2018; J. S. den Brok et al. 2023a). So far, only a small number of studies exist that systematically investigate the CO line ratio across a sample of nearby galaxies (A. K. Leroy et al. 2009, 2013, 2022; J. S. den Brok et al. 2021; Y. Yajima et al. 2021; R. P. Keenan et al. 2025, 2024). A major limitation of these studies, however, remains that in the case of single-dish observations, calibration uncertainties can introduce significant scatter in subsequent CO line measurement (see discussion in J. S. den Brok et al. 2021). Moreover, if observations from different telescopes are used to compute the CO line ratio, uncertainties in aperture correction constitute an additional point of scatter. Since the dynamical range of R_{21} is small (with values at the kiloparsec-scale ranging generally from 0.5–0.9 in nearby star-forming galaxies), the uncertainties can potentially dominate and hence explain the large scatter reported in the literature. Currently, the interferometer at ALMA is the only facility that can provide the high sensitivity and low calibration uncertainty that are crucial for such a study. The cycle 11 ALMA technical handbook quotes a flux calibration uncertainty of ∼5% for band 3 and band 6 observations (see A. Remijan et al. 2019). We discuss the ALMA flux calibration uncertainty in more detail in Section 2.2.3.

In this study, we present Cycle 9 ALMA 7 m+TP CO(1–0) observations of a set of 12 nearby star-forming galaxies (project code: 2022.1.01479.S; PI: J. den Brok). In addition, we include two more archival ALMA CO(1–0) mapping

[15] The reason for this is the high sensitivity of the Band 6 receiver (which covers the CO(2–1) line) and that to reach similar resolution, a configuration with longer baselines needs to be chosen for CO(1–0), leading to a sparser u–v sampling.

observations: NGC 3627 (2015.1.01538.S, PI: R. Paladino; J. S. den Brok et al. 2023b) and NGC 5236 (2017.1.00079.S, PI: J. Koda; J. Koda et al. 2023). In combination with the CO(2–1) ALMA observations as part of the PHANGS survey (A. K. Leroy et al. 2021b), we have a set of 14 galaxies for which we study the resolved R_{21} at 1.7 kpc physical resolution. The main science questions that we address are as follows:

1. To what degrees do varying physical conditions in the gas, and uncertainties in the relative flux calibration contribute to previously observed galaxy-to-galaxy scatter in R_{21}?
2. What magnitude of variations does R_{21} exhibit at 1.7 kpc physical resolution contrasting different dynamical environments, including galaxy centers against disks, and spiral arms against interarm regions?
3. How well do local conditions, e.g., the SFR surface density, predict R_{21} in nearby galaxies and what are the best current scaling relations to estimate this quantity?

This paper is structured as follows: In Section 2, we describe the properties of the sample of 14 galaxies, the observations and reduction of the new ALMA CO(1–0) data, and the approach used to homogenize the full data set for the science analysis. We describe our methods in Section 3. In Section 4, we present the main results, including the overall distribution of R_{21} across all sight lines and the variation of R_{21} within individual galaxies. We discuss the science questions and relate our findings to previous studies in Section 5 and conclude in Section 6.

2. Data and Observations

2.1. The Sample

In order to achieve a systematic analysis of the CO line ratio variation across and within a sample of nearby star-forming galaxies, we analyze targets for which ALMA observations exists for both the CO(1–0) and CO(2–1) emission line. A robust benchmark of the CO line ratio R_{21} requires a representative sample of the nearby star-forming galaxy population. This current study is based on a pilot proposal targeting 14 galaxies drawn from the PHANGS–ALMA survey sample of 90 galaxies for which ALMA 12 m CO(2–1) observations exist. The selection for this pilot sample was aimed at ensuring a good dynamic range in galactic SFR and stellar mass. For 12/14 galaxies, ALMA 7 m+TP observations were obtained as part of cycle 9 (project code: 2022.1.01479.S, P.I.: J. den Brok). In addition, we include two galaxies from the PHANGS sample for which ALMA CO(1–0) and CO(2–1) already exist in the archive. The left panel in Figure 1 illustrates the distribution of the selected galaxies in the SFR–$M_\star$ parameter space. The figure shows that our targets span more than a factor of 10 in stellar mass, $M_\star$, and SFR. They span a smaller but still significant range in specific SFR or offset from the main sequence of star-forming galaxies. All galaxies in our sample are within a distance of $D < 25$ Mpc, resulting in an achievable physical resolution (based on the angular resolution of the ALMA 7 m+TP observations) of less than or equal to 1.7 kpc (see right panel of Figure 1). For reference, Table 1 lists the galaxy properties of our sample.

2.2. ALMA Observations

2.2.1. Cycle 9 ALMA 7 m and TP Observations and Data Reduction

This paper presents new Band 3 ALMA CO(1–0) observations of 12 nearby galaxies (Table 1). The observations are part of Cycle 9 project 2022.1.01479.S. We observed the CO(1–0) line, rest frequency 115.271 GHz, using both the total power (TP) and seven meter array (7 m) portions of the Morita Atacama Compact Array (ACA). After processing and convolution to a circular synthesized beam, the final observations achieved an angular resolution of approximately 14″–15″. Because we include TP observations, we ensure that no flux is missing. All observations were carried out between 2022 September and 2023 November.

We adopted the observatory provided pipeline for the calibration of the CO(1–0) data, which used CASA (v6.4.1) and the ALMA calibration pipeline (CASA Team et al. 2022; T. R. Hunter et al. 2023). Our quality assurance did not reveal any issues with the pipeline, and the data did not require any manual flagging.

We used the PHANGS–ALMA pipeline[16] to image the calibrated data and produce science-ready data cubes. For a detailed description of the pipeline's functionalities and methods, we refer to the dedicated paper A. K. Leroy et al. (2021a) or the concise description in Appendix A of D. Liu et al. (2023). In short, the imaging pipeline goes through the following steps: (i) visibility data are converted to a user-defined channel width and frequency range such that the targeted emission line is well sampled; (ii) the continuum is subtracted using a zeroth-order polynomial; (iii) the image is cleaned using the repeated CASA `tclean` function, emphasizing frequent "major cycles" (i.e., frequent re-calculation of the model and residuals in the visibility domain). The routine performs a multiscale cleaning down to $\sim 4\sigma$ followed by a single-scale cleaning down to $\sim 1\sigma$ focused on regions with detected signal. Imaging is considered to converge when successive calls to clean show little influence on the total flux in the model. (iv) Finally, the pipeline performs a series of post-processing steps, which include primary-beam correction, conversion of the cube units to brightness temperature expressed in kelvin, short-spacing correction using CASA's `feather` task, and finally convolution of the channels to a common, circularized beam. Figure 2 presents an overview of the resulting CO(1–0) moment-0 maps.

In addition to our new observations, our analyses use archival CO(1–0) data sets, Project 2015.1.01538.S (P.I. R. Paladino) targeting NGC 3627 and Project 2017.1.00079.S (P.I J. Koda) targeting NGC 5236 (M83). Both projects include ACA 7 m and TP observations, which we process and image in an identical way as the new data. Figure 2 also shows these targets convolved to a synthesized beam size of 15″ to match our other data.

Table 1 lists the achieved CO(1–0) sensitivities at 2.5 km s^{-1} channel width for the working resolution (1.7 kpc) and at native resolution. At 1.7 kpc angular resolution, the sensitivity ranges from 1–16 mK, with most of the sources (11/14) having a sensitivity of <10 mK. Assuming $\alpha_{\rm CO(1-0)} = 4.35\,M_\odot\,{\rm pc}^{-2}/({\rm K\,km\,s^{-1}})$, this translates to a 3σ molecular gas surface density sensitivity of $\lesssim 3\,M_\odot\,{\rm pc}^{-2}$ (assuming a CO(1–0) FWHM of 20 km s^{-1}).

[16] v3.1; https://github.com/akleroy/phangs_imaging_scripts.

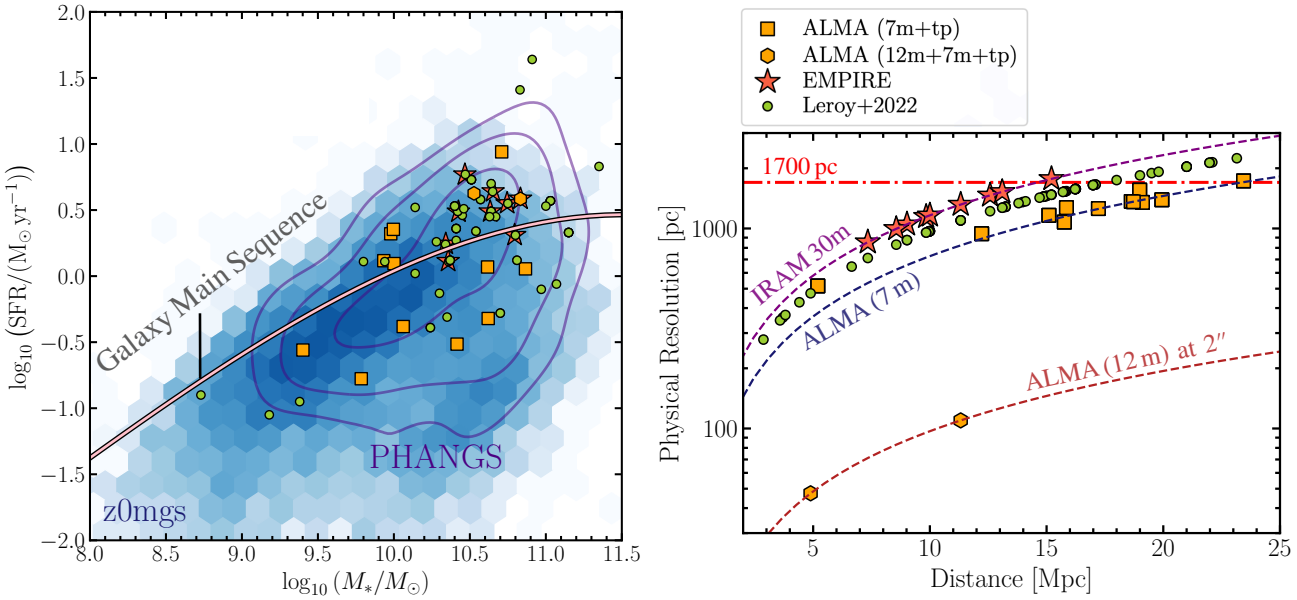

Figure 1. Sample overview. Left panel: shown here is the distribution of studied galaxies in the SFR–M_* parameter space. The orange squares and hexagons indicate the 14 galaxies that form our sample. For reference, the red stars present the nine sources analyzed as part of the EMPIRE CO line ratio paper (J. S. den Brok et al. 2021). The green circles represent the galaxies for which A. K. Leroy et al. (2022) presented R_{21} measurements. For context, the contour lines show the 90%, 75%, and 33% inclusion region of PHANGS galaxies in the SFR–M_* parameter space (A. K. Leroy et al. 2021b). The blue underlying density distribution illustrates the sample of galaxies within $d < 50$ Mpc ($N_{\rm gal} \approx 11{,}000$; A. K. Leroy et al. 2019). The gold and black line illustrates the galaxy main sequence at $z = 0$ following the parameterization from A. Saintonge et al. (2017). Right panel: illustrated here is the achievable physical resolution based on the observed angular resolution and the galaxy's measured distance. The points follow the description of the left panel. The red, blue, and purple dashed lines indicate the achievable physical resolution as a function of the galaxy's distance for ALMA 12 m, ALMA 7 m, and IRAM 30 m observations. We perform the subsequent analysis at a common physical resolution of 1.7 kpc, which is illustrated by the red dashed–dotted horizontal line. We note that for the ALMA 12 m array, multiple configurations are possible that lead to even higher angular (and hence physical) resolutions.

Table 1
Sample of Cycle 9 ALMA CO(1–0) Observations

Galaxy	i (deg)	P.A. (deg)	Distance (Mpc)	$\log_{10} M_\star$ ($M_\odot$)	$\log_{10}$ SFR ($M_\odot$ yr^{-1})	AGN	Beam[a] (″)	$\langle\sigma^{12}_{\rm CO(1-0)}\rangle$[b] (mK)	$\langle\sigma^{12}_{\rm CO(2-1)}\rangle$[c] (mK)	Ap. Corr.[d]
NGC 0685	23.0	100.9	19.94	10.06	−0.38	✗	17.6/(14.4)	12.9/(17.6)	2.7	1.2
NGC 1087	42.9	359.1	15.85	9.93	0.12	✗	22.1/(16.5)	7.4/(11.9)	1.7	1.0
NGC 1300	31.8	278.0	18.99	10.61	0.069	✗	18.5/(16.9)	9.7/(12.5)	2.4	1.1
NGC 1317	23.2	221.5	19.11	10.62	−0.32	✗	18.3/(14.6)	11.3/(18.3)	1.7	1.1
NGC 1385	44.0	181.3	17.22	9.98	0.32	✗	20.4/(15.1)	8.0/(15.1)	1.7	1.0
NGC 1433	28.6	199.7	18.63	10.87	0.055	✗	18.8/(15.1)	9.9/(15.5)	3.2	1.2
NGC 2566	48.5	312.0	23.44	10.71	0.94	✗	15.2	16.1	3.9	1.0
NGC 2835	41.3	1.0	12.22	10.00	0.095	✗	28.7/(15.9)	6.0/(16.2)	2.0	1.4
NGC 3627*	57.3	173.1	11.32	10.83	0.58	✓	30.4/(4.5)	6.7/(55.7)	1.6	1.3
NGC 4457	17.4	78.7	15.10	10.41	−0.51	✗	23.2/(15.9)	9.1/(17.7)	2.8	1.0
NGC 4540	28.7	12.8	15.76	9.79	−0.77	✗	22.2/(14.1)	12.1/(27.6)	3.8	1.0
NGC 5068	35.7	342.4	5.20	9.40	−0.56	✗	67.4/(20.5)	1.8/(31.4)	1.2	1.3
NGC 5236*	24.0	225.0	4.89	10.53	0.63	✗	71.7/(3.5)	1.0/(44.8)	0.3	1.1
NGC 7496	35.9	193.7	18.72	10.00	0.35	✓	18.7/(15.0)	8.5/(13.0)	2.1	1.0

Notes. (*) Not part of cycle 9 program, but ALMA CO(1–0) and CO(2–1) observations available.
[a] This corresponds to the FWHM of the circularized beam for the working resolution (i.e., physical resolution of 1.7 kpc) and native resolution in parentheses. (∼1.7 kpc), and the native resolution is in the brackets. For NGC 2566, the working resolution corresponds to the native resolution.
[b] The average channel rms at 2.5 km s^{-1} for CO(1–0) at working and native (in parentheses) angular resolution.
[c] The average rms noise per channel at 2.5 km s^{-1} for PHANGS–ALMA CO(2–1) at working resolution.
[d] The aperture correction based on the Wide-field Infrared Survey Explorer (WISE) band 3 flux.
Sources: Galaxy orientation taken from P. Lang et al. (2020). Galaxy distance drawn from G. S. Anand et al. (2021). The galaxy-integrated SFR and stellar mass are adopted from A. K. Leroy et al. (2022).

2.2.2. PHANGS–ALMA CO(2–1) Data

We combine our CO(1–0) ALMA observations with CO(2–1) data from the PHANGS–ALMA survey (A. K. Leroy et al. 2021b). The set of CO(2–1) observations include 12 m+7 m+TP ALMA data, ensuring no missing flux due to lack of undersampling of short baselines. We use first public release (team version 4) of the PHANGS–ALMA data products (A. K. Leroy et al. 2021a). Though PHANGS–ALMA includes 7 m+TP only data products, we use the 12 m+7 m

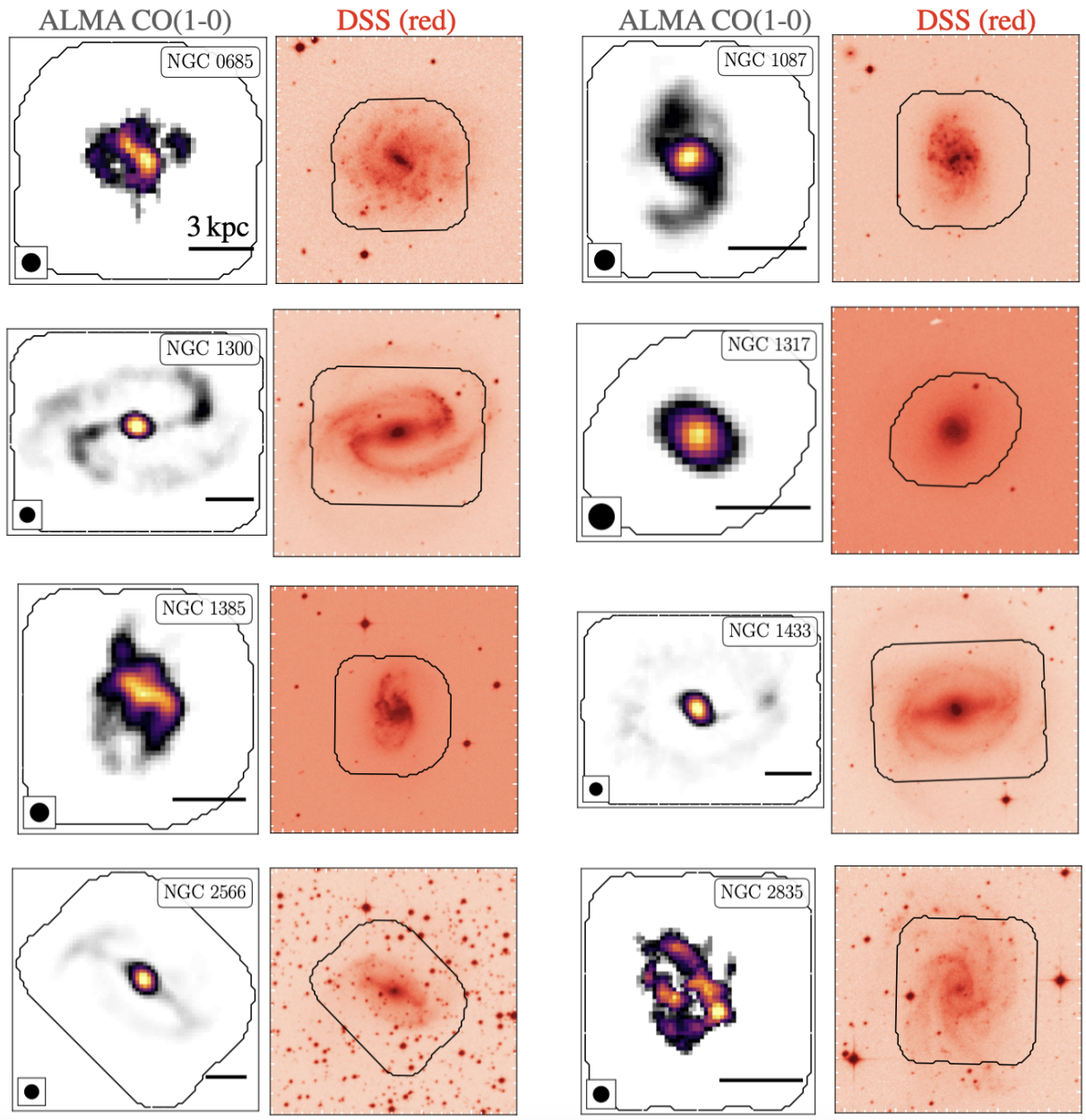

Figure 2. ALMA CO (1–0) moment-0 maps The panel with the galaxy name label in the top-right corner present the CO(1–0) observations at the native ALMA 7 m resolution (∼15″). The black circle shows the beam size, and the black line indicates a physical scale of 3 kpc, when accounting for the galaxy's distance. For NGC 3627 and NGC 5236, higher angular resolution data is available, but we convolved the maps to 15″ for consistency in the presentation. The panels in red to the right illustrate the DSS red maps for reference. The black contour represent the outline of the CO(1–0) ALMA observations.

+TP products and convolve them to our working resolution. We note that the data have been calibrated, processed, and imaged using the same approach that we use for the CO(1–0) ALMA data. We expect these to represent the highest-quality, most accurate set of CO(2–1) maps provided by the survey. After convolution to matched resolution, the PHANGS–ALMA CO(2–1) data have typical noises of <4 mK at 2.5 km s^{-1} channel width. Therefore, the CO(2–1) data surpasses the CO(1–0) data in terms of sensitivity by a factor of 2–4 for each galaxy (for a comparison, we refer to Table 1).

2.2.3. ALMA Calibration Uncertainty and Total Flux Recovery

A key requirement for successfully benchmarking the R_{21}^{12} variation is a robust flux calibration with low uncertainty. ALMA regularly monitors quasars and hence can achieve a total power calibration with gain uncertainties at Band 6 frequencies around 5%–10% and Band 3 frequencies around 5% as stated in the ALMA technical notes (see A. Remijan et al. 2019). Analyzing the TP observations for PHANGS–ALMA, including the galaxies that we study here, A. K. Leroy et al. (2021a) reported a low rms of 2%–4% rms variation of the intensity among repeat observations of a given high signal-to-noise ratio (S/N) source across different dates. They also showed good overall agreement between the PHANGS–ALMA CO (2–1) maps and previous IRAM 30 m mapping, with the cases of poor agreement attributable to known issues with the IRAM 30 m data (see also J. S. den Brok et al. 2021). L. Francis et al. (2020) reported even lower flux calibration

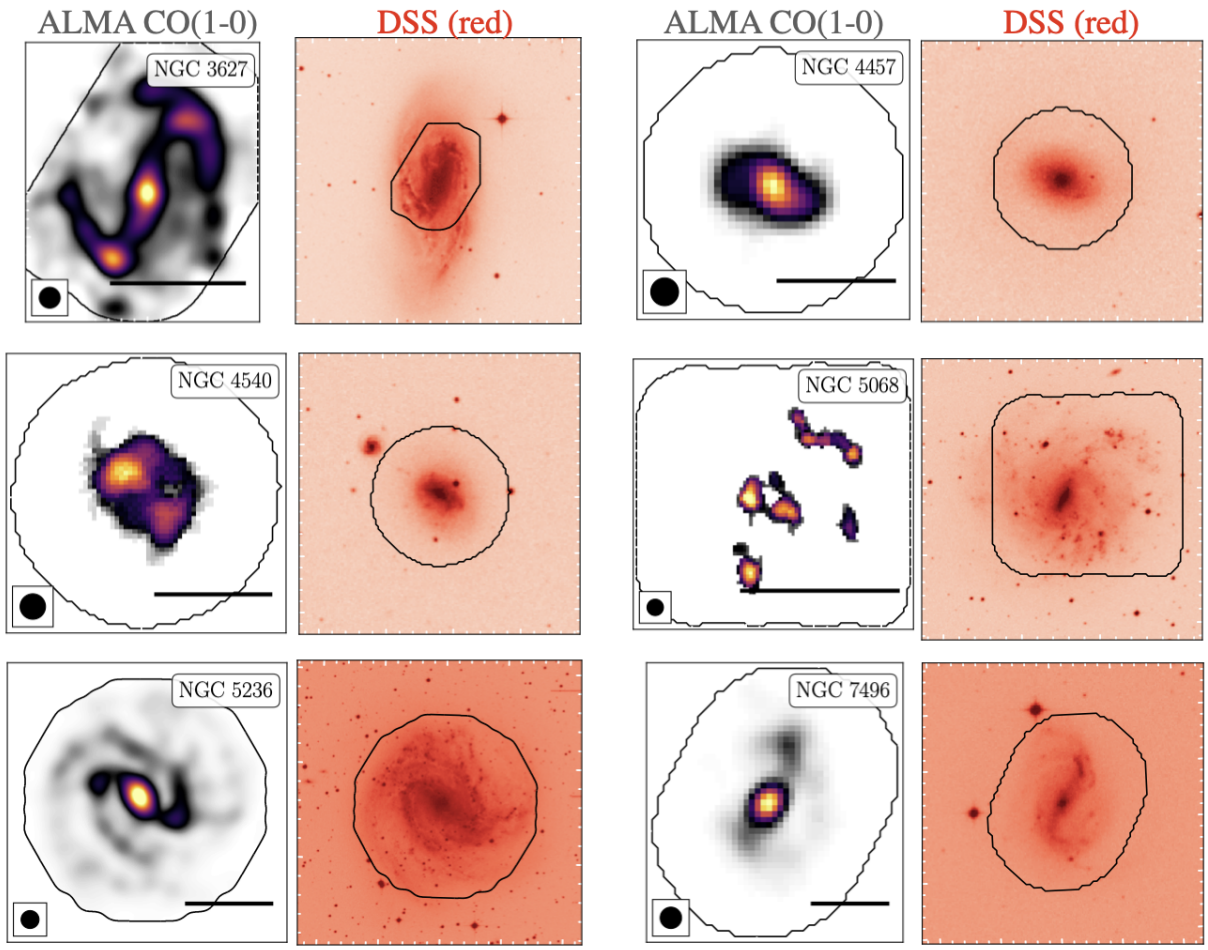

Figure 2. (Continued.)

uncertainties, with only ∼1% for Band 3 observations for a carefully selected spectral setup. Therefore, we infer a conservative estimate of a ∼5% flux calibration uncertainty for the ALMA data. We note that this 5% uncertainty is significantly lower than the calibration uncertainty reported for IRAM 30 m CO mapping observations using the EMIR (10%–15%; J. S. den Brok et al. 2021) or HERA ($\lesssim$20% based on a detailed analysis in A. K. Leroy et al. 2009; J. S. den Brok et al. 2021) receivers. This is also much less than the uncertainty associated with the Nobeyama 45 m COMING survey, for which Y. Yajima et al. (2021) cited a combined calibration and pointing uncertainty of 25%.

ALMA is constructed with the goal of recovering the true sky intensity via the inclusion of 7 m and TP observations. However, all astrophysical interferometers have some incomplete *u*–*v* coverage, and this will have an effect on the final flux recovery. For PHANGS–ALMA, A. K. Leroy et al. (2021a) and L. Neumann et al. (2023a) gauged the uncertainty associated with *u*–*v* sampling and image reconstruction on the output image by running simulated galaxy images through the PHANGS–ALMA data processing pipeline (A. K. Leroy et al. 2021a) and then applying spectral stacking techniques (L. Neumann et al. 2023a). They found that when the TP data are included, the majority of the signal of millimeter line emission across galaxies is recovered by the 7 m+TP observations within 10% and often much better. Our conclusions still hold even when assuming a higher uncertainty of ∼10%. For reference only, given the detailed investigations by A. K. Leroy et al. (2021a) and L. Neumann et al. (2023a), we show the overlap in *u*–*v* space for CO(1–0) and CO(2–1) for one galaxy in our sample in Appendix A to demonstrate that we have sufficient overlap to recover the CO fluxes.

2.3. Ancillary Data Sets

In this study, we require additional multiwavelength observations to correlate the CO line ratio with various galactic properties. Here, we briefly describe the origin and products of the key supplementary data sets.

2.3.1. SFR and Stellar Mass Surface Density

In order to obtain matched-resolution star formation and stellar mass surface density estimates, we use a combination of narrowband Hα and Wide-field Infrared Survey Explorer (WISE) 22 μm data. The narrowband Hα have been acquired with the 2.5 m du Pont telescope and the ESO/MPG 2.2 m telescope (see A. Razza et al. 2024, in preparation). And the WISE data are part of the z0mgs survey products (A. K. Leroy et al. 2019). The combination of the optical and infrared flux and subsequent conversion to a star formation ratio follows the new calibration presented in F. Belfiore et al. (2023). This prescription is better adapted at minimizing the contamination

from the infrared cirrus in the 22 μm band than the commonly used D. Calzetti et al. (2007) prescription.

The stellar mass surface density, Σ_*, is estimated using Spitzer IRAC 3.6 μm near-infrared (NIR) maps (G. G. Fazio et al. 2004; most from S4G K. Sheth et al. 2010). We refer to A. K. Leroy et al. (2021b) for a detailed description of the approach used to estimate the stellar mass surface density. In short, the NIR image is converted to a stellar mass surface density using a mass-to-light ratio that depends on an observed color related to the local specific SFR. In practice, the mass-to-light ratio is calculated based on the ratio of the SFR and the WISE1 (3.4 μm) band using a scaling relationship calculated by A. K. Leroy et al. (2019) to match the results of population synthesis modeling of the Sloan Digital Sky Survey main galaxy sample by S. Salim et al. (2016, 2018). That modeling adopted the G. Bruzual & S. Charlot (2003) stellar population models and assumes a G. Chabrier (2003) initial mass function. The resulting stellar mass estimates are overall consistent with population synthesis model of the PHANGS–MUSE data and are consistent with previous studies, such as A. K. Leroy et al. (2022).

2.3.2. Metallicity

For eight of our 14 targets, we use metallicity measurements obtained from PHANGS–MUSE observations (E. Emsellem et al. 2022).[17] For the analysis related to the metallicity, we therefore drop the remaining six galaxies and only focus on the sample of eight for which measurements are available. We specifically use the metallicity maps from T. G. Williams et al. (2022). The 2D metallicity distribution is determined using a Gaussian process regression by extrapolating measurements of individual pointings within the galaxies and the radial trends. The metallicities for individual pointings are estimated using the S-calibration system of L. S. Pilyugin & E. K. Grebel (2016). See B. Groves et al. (2023) for more discussion of the metallicity estimates for PHANGS–MUSE.

2.4. Homogenizing and Processing the Data

To ensure a systematic analysis, we convolve the cubes to a common physical resolution of 1.7 kpc using a Gaussian beam size and regrid to a hexagonal grid. We use the publicly available `PyStructure` pipeline[18] (J. den Brok et al. 2024), which has been employed in previous studies (e.g., J. S. den Brok et al. 2021; C. Eibensteiner et al. 2022; L. Neumann et al. 2023b). This versatile tool allows for the combination of a set of different 3D data cubes and 2D maps from different telescopes and at different frequencies into a common data structure. All data are then convolved to a user-defined angular (or physical) resolution and regridded to the same grid using a user-defined prior cube. The points of the resulting grid are half-beam spaced in a hexagonal pattern. This pattern optimizes the oversampling with respect to the commonly used Cartesian grid. The pipeline also deprojects the coordinates using the position angle, inclination, and distance of the individual galaxies. This way, we can compute the galactocentric radius of each sight line as well as the Vaucouleurs radius (r_{25}).

The pipeline then performs a post-processing of the 3D data cubes and computes the moment maps. To integrate, the tool first determines a velocity range based on a user-defined prior line. In our case, we select the CO(2–1) emission line due to its higher S/N than the CO(1–0). The signal mask over the entire cube is then determined using a method adapted from A. K. Leroy et al. (2021a). For the creation of the signal mask, first, the noise is determined along both the spatial and spectral dimensions over the signal-free part of the cube using the `mad_std` function from `astropy`. This function computes the median absolute deviation. A factor of 1.4826 is then applied to convert it into a standard deviation assuming a Gaussian distribution of the noise. Then, the pipeline first selects all voxels that satisfy the high (4σ) S/N threshold. In a next step, the resulting signal mask is expanded to include all adjacent voxels that are contained within the lower (2σ) S/N mask. Finally, the signal mask is extended along the velocity axis by another 10 km s^{-1}.

The resulting signal mask is then applied to compute the peak intensity, the integrated intensity (moment-0), the velocity weighted mean (moment-1), and the velocity dispersion (in terms of FWHM). We note that the moment-1 and moment-2 calculations are sensitive to noise effects. Therefore, an additional signal mask is computed for each line separately for the purpose of the moment-1 and moment-2 per line only. This mask is hence not based on the brighter or higher-S/N prior line. The pipeline also computes the uncertainty of the moment maps by propagating the rms it determines from the signal-free part of the spectrum. The precise calculation follows the prescriptions from A. K. Leroy et al. (2021a).

We also provide aperture correction values for the global (galaxy-wide) measurements as our field of view of the CO(1–0) and CO(2–1) observations generally do not cover the entire disk of the galaxy, but are limited to the region active with star formation. We expect to cover most of the CO flux within our observed field of view, but note that fainter CO emission might extend into the outer disks of galaxies (see, for example, J. S. Young et al. 1995; J. Braine et al. 2007; A. Schruba et al. 2011). To quantify the corresponding *aperture* correction, we follow the approach outlined in A. K. Leroy et al. (2021a). The method consists of taking the ratio of the WISE band 3 flux summed over the entire galaxy with repsect to the flux within the field of view of our ALMA observations. The motivation for taking the band WISE 3 data is that a close correlation exists with the CO integrated intensity (for more details, see A. K. Leroy et al. 2021a).

3. Line Ratio Measurements

3.1. Resolved CO Line Intensity Ratio

We measure the ratio for each 1.7 kpc physical scale resolved line of sight. In particular, we define the integrated line intensity ratio as

$$R_{21} \equiv R_{21}^{1.7\,\mathrm{kpc}} = \frac{W_{\mathrm{CO}}^{2\rightarrow1}}{W_{\mathrm{CO}}^{1\rightarrow0}} \quad (1)$$

where $W_{\mathrm{CO}}^{2\rightarrow1}$ and $W_{\mathrm{CO}}^{1\rightarrow0}$ represent the moment-0 value as extracted from the `PyStructure` (see Section 2.4) in units of K km s^{-1} at 1.7 kpc physical resolution. For reference, we note that in our line ratio framework, the line ratio for an

[17] The sample of galaxies for which we have MUSE-IFU observations are: NGC 1087, NGC 1300, NGC 1385, NGC 1433, NGC 2835, NGC 3627, NGC 5068, and NGC 7496.

[18] https://github.com/jdenbrok/PyStructure

Table 2
Summary of Line Ratio Results (Highlighted in Bold Is the Recommended Value to Use for a Sample of Galaxies)

	Resolved						Unresolved	
				$\langle R_{21}\rangle$				
Galaxy	$n_{\rm pixel}$	$f^{\geqslant 5S/N}_{CO(1-0)}$	$f^{\geqslant 5S/N}_{CO(2-1)}$	Entire Map	Center	Disk	$\langle R_{21}\rangle_{\Sigma}$	$\langle R_{21}\rangle_{\rm stacked}$
NGC 0685	71	80%	76%	$0.70^{+0.10}_{-0.10}$	$0.67^{+0.10}_{-0.13}$	$0.70^{+0.11}_{-0.10}$	$0.74^{+0.05}_{-0.05}$	$0.82^{+0.06}_{-0.06}$
NGC 1087	116	98%	98%	$0.75^{+0.10}_{-0.10}$	$0.78^{+0.04}_{-0.05}$	$0.73^{+0.13}_{-0.10}$	$0.76^{+0.05}_{-0.05}$	$0.78^{+0.06}_{-0.06}$
NGC 1300	343	98%	97%	$0.53^{+0.09}_{-0.11}$	$0.63^{+0.13}_{-0.06}$	$0.52^{+0.09}_{-0.10}$	$0.56^{+0.04}_{-0.04}$	$0.55^{+0.04}_{-0.04}$
NGC 1317	39	99%	98%	$0.83^{+0.29}_{-0.24}$	$0.83^{+0.22}_{-0.13}$	$0.69^{+0.46}_{-0.22}$	$0.83^{+0.06}_{-0.06}$	$0.85^{+0.06}_{-0.06}$
NGC 1385	128	98%	98%	$0.76^{+0.11}_{-0.13}$	$0.77^{+0.03}_{-0.04}$	$0.75^{+0.13}_{-0.13}$	$0.78^{+0.06}_{-0.06}$	$0.78^{+0.06}_{-0.06}$
NGC 1433	309	97%	96%	$0.56^{+0.09}_{-0.09}$	$0.65^{+0.10}_{-0.09}$	$0.56^{+0.09}_{-0.09}$	$0.61^{+0.04}_{-0.04}$	$0.60^{+0.04}_{-0.04}$
NGC 2566	277	99%	98%	$0.63^{+0.22}_{-0.13}$	$0.85^{+0.46}_{-0.21}$	$0.63^{+0.19}_{-0.13}$	$0.73^{+0.05}_{-0.05}$	$0.71^{+0.05}_{-0.05}$
NGC 2835	84	97%	95%	$0.79^{+0.17}_{-0.09}$	$0.77^{+0.07}_{-0.10}$	$0.81^{+0.19}_{-0.09}$	$0.81^{+0.06}_{-0.06}$	$0.78^{+0.06}_{-0.06}$
NGC 3627	97	99%	98%	$0.62^{+0.11}_{-0.13}$	$0.71^{+0.04}_{-0.05}$	$0.60^{+0.12}_{-0.12}$	$0.64^{+0.05}_{-0.05}$	$0.63^{+0.04}_{-0.04}$
NGC 4457	37	99%	99%	$0.79^{+0.13}_{-0.16}$	$0.81^{+0.13}_{-0.10}$	$0.72^{+0.13}_{-0.14}$	$0.82^{+0.06}_{-0.06}$	$0.80^{+0.06}_{-0.06}$
NGC 4540	36	100%	100%	$0.65^{+0.03}_{-0.06}$	$0.65^{+0.03}_{-0.04}$	$0.65^{+0.04}_{-0.07}$	$0.65^{+0.05}_{-0.05}$	$0.67^{+0.05}_{-0.05}$
NGC 5068	25	100%	100%	$0.80^{+0.04}_{-0.07}$	$0.80^{+0.03}_{-0.05}$	$0.80^{+0.04}_{-0.07}$	$0.79^{+0.06}_{-0.06}$	$0.78^{+0.06}_{-0.06}$
NGC 5236	132	100%	100%	$0.73^{+0.04}_{-0.05}$	$0.79^{+0.02}_{-0.04}$	$0.73^{+0.04}_{-0.05}$	$0.76^{+0.05}_{-0.05}$	$0.76^{+0.05}_{-0.05}$
NGC 7496	118	98%	98%	$0.73^{+0.20}_{-0.13}$	$0.68^{+0.22}_{-0.03}$	$0.73^{+0.20}_{-0.14}$	$0.79^{+0.06}_{-0.06}$	$0.80^{+0.06}_{-0.06}$
sample-wide	1812	99%	98%	$\mathbf{0.64^{+0.16}_{-0.14}}$	$0.75^{+0.09}_{-0.12}$	$0.63^{+0.17}_{-0.14}$	$0.70^{+0.05}_{-0.05}$	$0.71^{+0.05}_{-0.05}$

Note. For the resolved ratios, we list the median and 16th–84th percentile range.

optically thick and thermalized line will tend toward approximately unity[19] (P. M. Solomon & P. A. Vanden Bout 2005). When presenting results for individual sight lines and histograms or maps maps of the ratio, we include those sight lines for which both the CO(1–0) and CO(2–1) integrated intensities exceed an $S/N > 5$. We note that for all galaxies in our sample, the CO(2–1) is observed at higher sensitivity, so generally, the CO(1–0) is the limiting factor for whether a sight line is classified as significant (i.e., $S/N > 5$ for both lines) or not (see Table 1). Our signal clipped mask at $S/N > 5$ still contains the majority of the CO emission over the full galaxy. We compare the flux within the $S/N > 5$ mask to the flux across the entire map. We find a median completeness of the ALMA data across the sample of 98% for CO(1–0) and 96% for CO(2–1) (see Table 2 for completeness values per galaxy). We use the Gaussian error propagation to derive an estimate of the CO ratio uncertainty from the uncertainty of the individual integrated intensities, which incorporates the channel rms and a flux calibration uncertainty of 5% (see Section 2.2.3).

3.2. Calculating an Average CO Line Ratio

A key result of this study is measurements of the average R_{21} line ratio across or within certain parts of the galaxies and quantification of the corresponding scatter. We report the average value calculated through three different methods:

$\langle R_{21}\rangle$—The resolved line ratio average. This measurement corresponds to the area-weighted median, which means that we weight each sight line per bin equally. We describe the scatter taking the 16th–50th percentile as a 1σ interval below the median, corresponding to the quantiles of Gaussian distribution. Similarly, the 50th–84th percentile range is a 1σ interval above the median. We note that for this measurement, we only average over significantly detected R_{21} values.

$\langle R_{21}\rangle_{\Sigma}$—The ratio-of-sums that we obtain by summing over pixels of CO(1–0) and CO(2–1) integrated intensities and then taking the ratio of the two (following definition in A. K. Leroy et al. 2022). In the case where the area that we sum over covers the whole galaxy, this value would correspond to an unresolved galaxy measurement. In practice, we sum over all pixels where there is measured CO emission for both lines (see description of how we construct such a signal mask in Section 2.4). For this approach, we do not provide a percentile range but propagate the uncertainties of the individual intensities we sum over.

$\langle R_{21}\rangle_{\rm stacked}$—Spectrally stacked ratio. We also employ a spectral stacking method to improve the S/N and detect potential trends of R_{21} with various physical quantities. The spectral stacking method resembles the one detailed in A. Schruba et al. (2011) and its application and robustness for interferometric data that include short-spacing data has been documented in L. Neumann et al. (2023a). We use the tool `PyStacker`[20] to perform the spectral stacking. In short, the technique consists of binning sight lines by a parameter of interest. Each spectrum for each sight line is regridded along the velocity axis such that the local mean velocity corresponds to $0\,{\rm km\,s^{-1}}$. This allows us to coherently add spectra from different locations in the galaxy or even different galaxies within a bin. We average together all spectra in each bin along each channel to obtain a stacked spectrum for both CO(1–0) and CO(2–1). Both lines are integrated over the same (moment-0) mask, and then their ratio forms the stacked R_{21} measurement. In contrast to the

[19] As described in A. K. Leroy et al. (2022), cosmic microwave background effects and the Raleigh–Jeans approximation will result in slight deviations such that the thermalized line ratio will not exactly tend toward unity.

[20] https://github.com/PhangsTeam/PyStacker

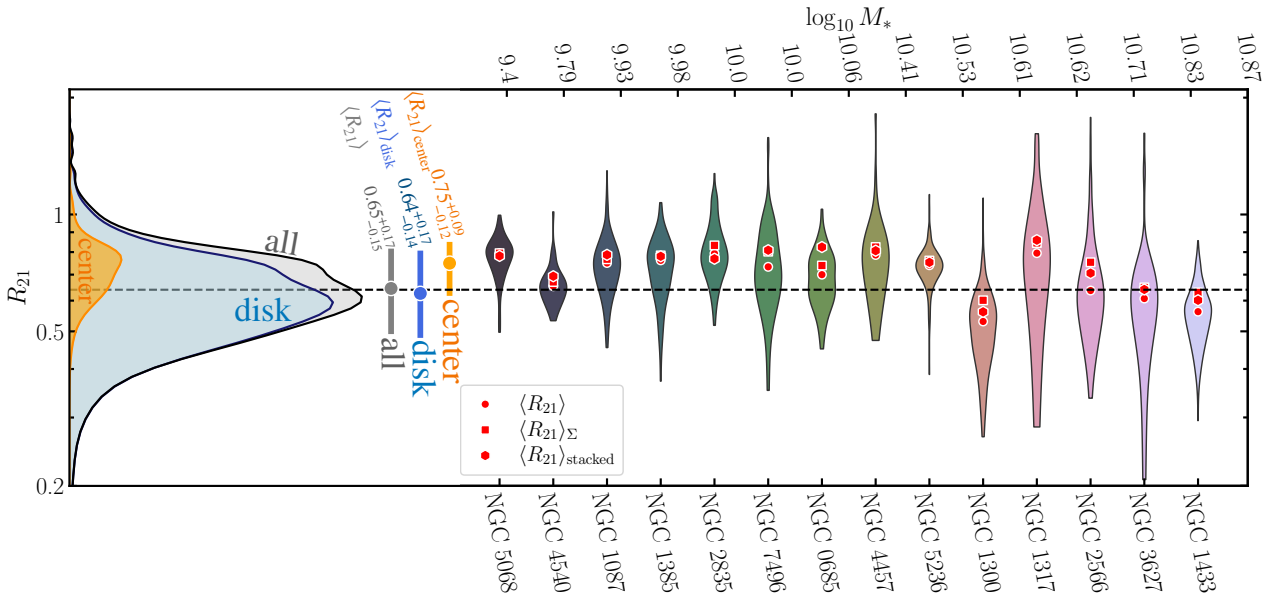

Figure 3. Sample-wide R_{21} distribution. Left panel: the kernel density estimation (KDE) of all significantly detected sight lines across the full galaxy sample. Here we also separate by sight lines associated with center (orange shaded region) and disk (cyan shaded region). For reference, we indicate the equally weighted (i.e., area-weighted) mean and 16th–84th percentile range of the three different KDEs in the top. Right panel: these violin plots show the distribution of R_{21} for sight lines with significant CO(2–1) and CO(1–0) detections for each galaxy. We illustrate the area-weighted median with a circle, the ratio-of-sum average with a square, and the stacked average with a hexagon marker. The dashed line indicates the sample-wide average when weighting all sight lines with significant line ratio detections equally.

binning of only significant detections described above, we apply this stacking to all sight lines. The difference between the two sets of results indicates how much faint undetected emission contributes to the overall results. Since a new mask over which to integrate is computed for each stacked spectral bin, the resulting ratio might vary slightly with resect to the ratio-of-sums, even in the case where all lines of sight within the bins have significant detected CO emission.

3.3. Binning CO Line Ratios

To highlight trends for the resolved sight lines across or within our sample of galaxies, we employ a binning analysis. For each parameter of interest, we define a set of bins (e.g., of $\Sigma_{\rm SFR}$, $r_{\rm gal}$, etc.) and group together all sight lines according to those bins. Then, within each bin, we perform the calculations of the average line ratios described in Section 3.2. We note that for the average ratio ($\langle R_{21}\rangle$), we only bin significant measurements, where both lines are detected at 5σ. In contrast, for the ratio of sums and stacking, we also included nondetections (i.e., $<5\sigma$) when binning.

We bin by four quantities: (i) galactocentric radius, $r_{\rm gal}$. (ii) The SFR surface density, $\Sigma_{\rm SFR}$. We bin by the value in units of $M_\odot\,{\rm yr}^{-1}\,{\rm kpc}^{-2}$ directly. (iii) The specific SFR, which is given by the ratio $\Sigma_{\rm SFR}/\Sigma_*$. (iv) The metallicity Z in terms of $12 + \log({\rm O/H})$. We note that we choose to bin by quantities that do not involve CO-derived values to avoid correlated axes.

4. Results

4.1. The Sample-wide R_{21} Distribution

In total, our post-processed data set consists of 1812 half-beam sampled sight lines[21] across the sample of 14 galaxies for which a significant R_{21} exists (i.e., ${\rm S/N} > 5$).

[21] Given an oversampling factor of ∼4, this corresponds to approximately ∼400 independent data points

4.1.1. Galaxy-scale Averages

The left panel in Figure 3 illustrates the overall distribution of significantly measured line ratios, and we report the corresponding statistics in Table 2. We find an area-weighted mean and 16th–84th percentile range across all sight lines of $\langle R_{21}\rangle = 0.64^{+0.16}_{-0.14}$. When we take the ratio of the sums of intensities across the galaxy and the stacked ratio, we get a higher average of $\langle R_{21}\rangle_\Sigma = 0.70^{+0.05}_{-0.05}$ and $\langle R_{21}\rangle_{\rm stacked} = 0.71^{+0.05}_{-0.05}$, respectively. The higher value of the average $\langle R_{21}\rangle$ likely reflects the fact that these averages constitute an intensity weighting and sight lines toward galaxy centers, which are intrinsically bright but represent few total sight lines, that tend to have higher R_{21}. This is also highlighted in the right panel of Figure 3 where the distribution of all sight lines is separated into disk and center. Here, the center is defined as sight lines with $r_{\rm gal} \leqslant 2$ kpc. Indeed, if only selecting the center sight lines, the average ratio (weighting all central sight lines equally) is even higher with $\langle R_{21}\rangle_{\rm center} = 0.75^{+0.09}_{-0.12}$.

In Figure 4 we illustrate the galaxy-wide median values plotted against key galaxy-integrated properties, such as the stellar mass, the SFR, and the specific SFR. With a Pearson correlation coefficient of $R_{\rm p} = -0.5$ (p-value of 0.05), we find that the galaxy-wide R_{21} seems to particularly scale with the stellar mass (and to a limited degree to the specific SFR). Physically, we expect these galaxy-averaged parameters to correlate with the average intensity of the radiation field, which in turn results in a stronger heating of the gas, driving up the line ratio. For instance, lower-mass galaxies tend to have higher sSFR, and hence a higher local $\Sigma_{\rm SFR}$. In addition, given the galaxy mass–metallicity relation (C. A. Tremonti et al. 2004; H. Lee et al. 2006), we expect lower-mass galaxies to have lower metallicities, resulting in a lower dust-to-gas ratio and hence more intense radiation fields. These effects could explain the observed anticorrelation with stellar mass and correlation with sSFR. Given the small number of galaxies within our sample, we caution, however, that individual outliers can affect the observed trends. For reference, we also

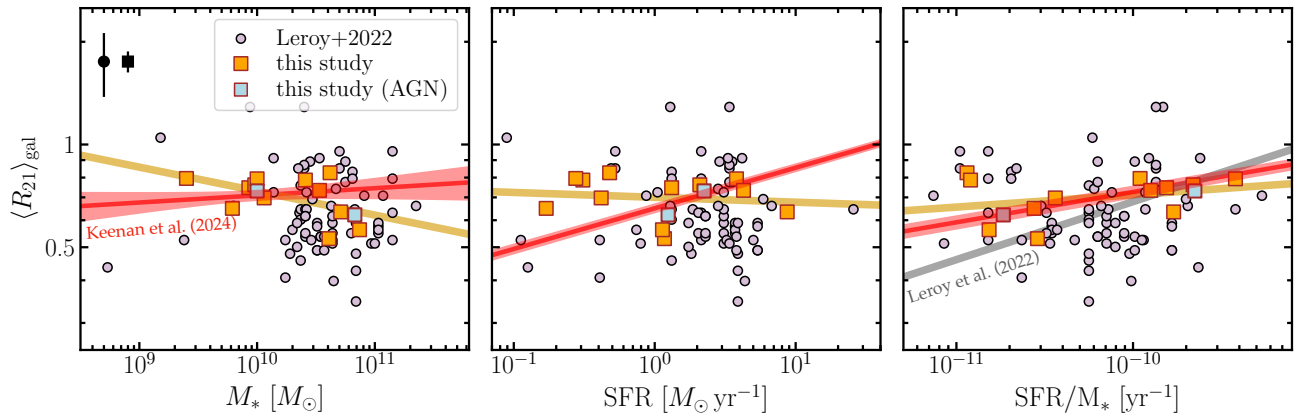

Figure 4. Trends of galaxy-wide R_{21} and galaxy-integrated properties. These panels illustrate the equally weighted median R_{21} per galaxy with respect to the galaxy-wide stellar mass, SFR, and specific SFR. For reference, we have included the sample of galaxies studied by A. K. Leroy et al. (2022). We perform a power-law regression to our sample of 14 galaxies, which is indicated with the orange line. Two of the sources in our sample host an active galactic nucleus (AGN; NGC 3627 and NGC 7496; highlighted in blue). The typical error (dominated by calibration uncertainties) is illustrated in the top-left corner of the left panel. For reference, we also show the scaling relation fit reported by R. P. Keenan et al. (2024; shown in red) and A. K. Leroy et al. (2022; shown in gray, and is available only for the SFR/$M_\star$).

include the individual galaxy-wide measurements from A. K. Leroy et al. (2022). We also include their reported scaling relation for SFR/M_* as well as the trends for the three quantities as derived by R. P. Keenan et al. (2024). Regarding the individual galaxy-integrated values, it is evident that our sample of measurements shows a lower scatter. For the residual with the fitted line, we find a scatter of 0.05 dex for our ALMA-based observations versus 0.11 dex for the single-dish sample, despite covering a similar dynamical range in galaxy SFR and stellar mass. This likely reflects the superior flux calibration stability and improved signal-to-noise of ALMA-based CO line intensity measurements.

In our sample, we have two sources that host an active galactic nucelus (AGN; NGC 3627; A. D. Goulding & D. M. Alexander 2009; and NGC 7496, H. R. Schmitt et al. 2006). To see whether the AGN influences the galaxy-wide average, we highlight them in Figure 4 using a blue-colored marker. We do not find any clear evidence that the AGN affects the galaxy-wide CO line ratio median, as these points do not deviate in any significant way from the regression line or the sample-wide median. We note that any impact of the AGN on the molecular gas will be likely be limited to the central region of the galaxy. At our 1.7 kpc physical resolution, we therefore do not expect to see much impact from AGN because even our central beam will include GMCs that likely are not significantly affected by the AGN.

For reference, we also present the galaxy-wide average R_{21} in the SFR–M_* parameter space in Figure 5. Notably, the two early-type galaxies in the Green valley (NGC,1317 and NGC,4457) show elevated ratios (though this is not exclusive, as two main-sequence galaxies also exhibit similar values). Additionally, while there is an apparent trend of decreasing ratios with increasing stellar mass (see also Figure 4), it is important to note exceptions, particularly the presence of galaxies with higher ratios at both low and high stellar masses. This suggests that the relationship between R_{21} and stellar mass is more complex and requires multiparameter analysis to fully characterize for a future study.

4.1.2. Resolved Measurement

In Figure 6, we plot R_{21} as a function of galactocentric radius ($r_{\rm gal}$), SFR surface density ($\Sigma_{\rm SFR}$), the specific SFR

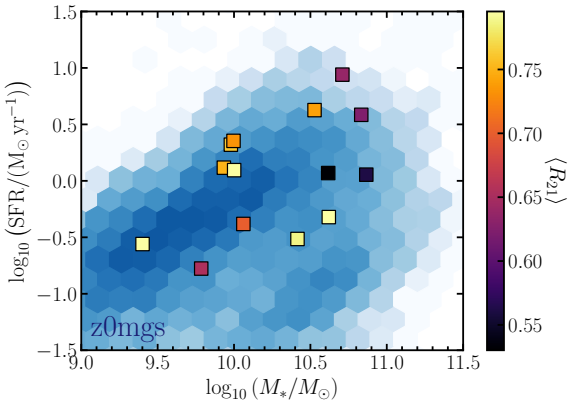

Figure 5. Distribution of galaxy-integrated $\langle R_{21}\rangle$ in the SFR–M_* parameter space The 14 galaxies in our sample are colored based on the galaxy-wide average R_{21} (see Table 2 for values). As reference, we illustrate also the z0mgs-sample distribution (see Figure 1).

surface density ($\Sigma_{\rm SFR}/\Sigma_\star$), and metallicity ($12 + \log_{10}$O/H; only for eight out of 14 targets in our sample). In these panels, we also show the binned medians (circles show equally weighted values, and squares show CO(1–0) intensity-weighted ones), and the vertical line illustrates the (equally weighted) 16th–84th percentile range per bin. In addition, we fit a regression line to the equally weighted binned means. For the regression line, we either assume a linear relation (galactocentric radius) or a power law[22] (SFR and specific SFR surface density). We provide an overview of the regression line coefficients in Table 3.

Galactocentric radius—Panel (a) of Figure 6 presents the correlation of the line ratio with galactocentric radius. We find a negative correlation, as indicated by the negative Kendall τ-value of -0.58 or -0.48 for the resolved R_{21} ratio median and the ratio of sums average, respectively (see Table 3). This trend is consistent with findings from high-resolution ($\sim$200 pc resolution) observations in NGC 3627 and NGC 2903, where

[22] We note that the correlations reported here only hold for the dynamical range of the observables. Beyond the covered range, we expect the ratio to behave differently, such as flattening toward unity and stabilizing around values of 0.3–0.5 (e.g., A. K. Leroy et al. 2022). See Appendix B for a comparison of different fitting prescriptions.

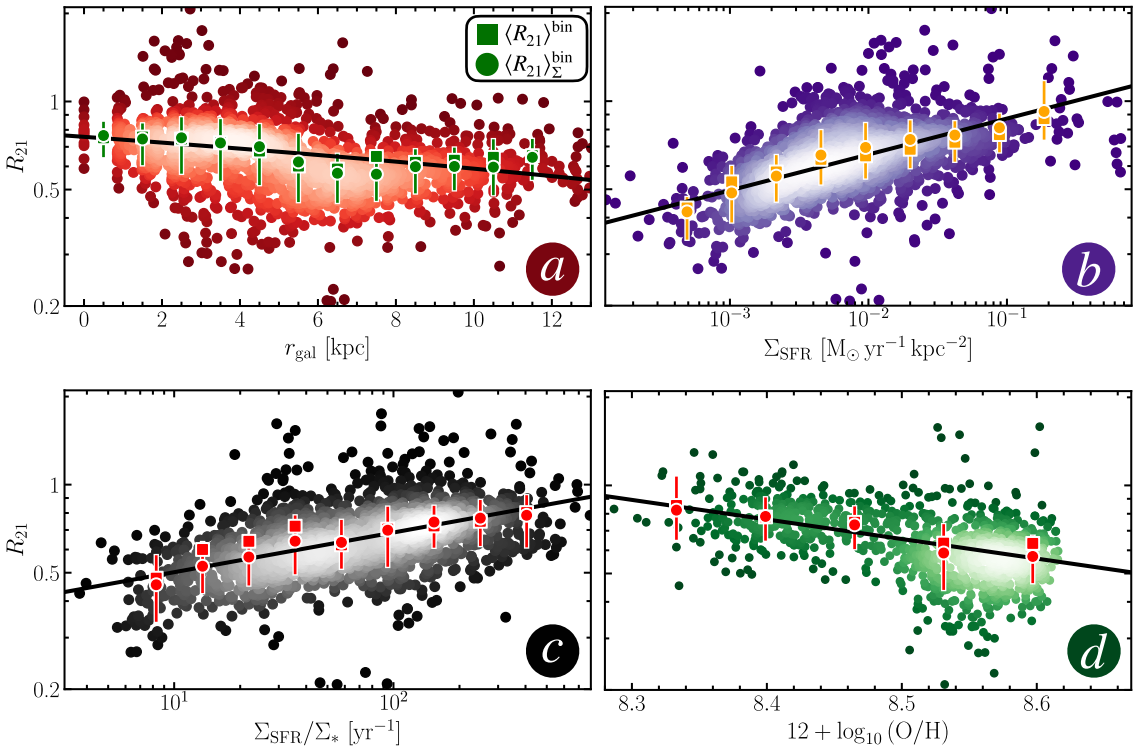

Figure 6. R_{21} correlation trends combining all sight lines The panels present the trends for the significantly detected sight lines. The points are color-coded using a density distribution function to illustrate where the majority of points lie within the respective parameter space. The larger markers with the error bars represent the binned means (circle: equally weighted; square: ratio-of-sums average). The error bars present the 16th–84th percentile range for individual significant measurements in that bin. Panel (a): the line ratio as function of galactocentric radius in kiloparsecs. Panel (b): the line ratio as function of SFR surface density, $\Sigma_{\rm SFR}$. Panel (c): the line ratio as function of the local specific SFR ($\Sigma_{\rm SFR}/\Sigma_*$). Panel (d): the line ratio as function of the metallicity, only for the eight (of 14) galaxies with available metallicity maps.

Table 3
Line Regression Results to Binned Trends in Figure 6

Average (y)	Quantity (x)	m	q	$\tau_{\rm Kendall}$
$\langle R_{21}\rangle$	$r_{\rm gal}$	$-0.017^{+0.006}_{-0.01}$	$0.76^{+0.08}_{-0.09}$	-0.58
$\langle R_{21}\rangle_\Sigma$		$-0.012^{+0.004}_{-0.004}$	$0.74^{+0.08}_{-0.09}$	-0.45
$\log_{10}\langle R_{21}\rangle$	$\log_{10}(\Sigma_{\rm SFR})$	$0.12^{+0.03}_{-0.04}$	$0.06^{+0.07}_{-0.09}$	1.0
$\log_{10}\langle R_{21}\rangle_\Sigma$		$0.10^{+0.02}_{+0.02}$	$0.01^{+0.05}_{-0.08}$	1.0
$\log_{10}\langle R_{21}\rangle$	$\log_{10}(\Sigma_{\rm SFR}/\Sigma_*)$	$0.14^{+0.03}_{-0.03}$	$-0.43^{+0.09}_{-0.13}$	0.94
$\log_{10}\langle R_{21}\rangle_\Sigma$		$0.10^{+0.03}_{-0.03}$	$-0.35^{+0.08}_{-0.10}$	0.83
$\langle R_{21}\rangle$	$12+\log_{10}({\rm O/H})$	$-1.1^{+0.8}_{-0.6}$	9^{+5}_{-8}	-1.0
$\langle R_{21}\rangle_\Sigma$		$-0.8^{+0.2}_{-0.2}$	8^{+6}_{-6}	-1.0

Note. We fit a linear regression of the form $y = mx + q$. We also provide the Kendall's τ correlation coefficient derived for the binned values.

the radial variation is particularly driven by the increase of R_{21} toward the center (J. S. den Brok et al. 2023b). We note that—qualitatively—from 6 kpc onward, R_{21} seems to rise again in contrast to the trend from 0–6 kpc. This is likely driven by NGC 1300, NGC 1433, and NGC 2566, which are the galaxies in our sample for which we have radial measurements beyond $r > 6$ kpc.

SFR surface density—Panel (b) of Figure 6 illustrates the correlation of R_{21} with the SFR surface density. We measure a significant positive correlation between the two quantities. We fit a power-law regression to the binned medians and report a positive correlation with a slope of $m = 0.12^{+0.03}_{-0.04}$ or $m = 0.10^{+0.02}_{-0.02}$, respectively, to the different binning techniques.

Local specific SFR—The bottom-right panel (c) of Figure 6 presents the correlation with the specific SFR along the sight line. For the correlation with the absolute line ratio, we find again a strong correlation with a Kendall's τ equal to 1 for the binned trend (see Table 3). The power-law regression for SFR surface densities in the 10^{-3}–$10^{-1}\,M_\odot\,{\rm yr}^{-1}\,{\rm kpc}^{-1}$ range yields a slope of $m = 0.14^{+0.03}_{-0.03}$ for the binned R_{21} median.

Metallicity—We only have metallicity maps for eight of 14 galaxies in our sample. In panel (d), we therefore only show sight lines for those eight galaxies. We also note that overall, we only cover a small dynamical range of metallicities ($\sim$0.25 dex); therefore, any real trends can potentially be hidden in the scatter of our measurements. For R_{21}, we measure a significant negative correlation with the metallicity with a Kendall's τ correlation coefficient of -1 (see Table 3). The linear regression through the binned medians yields a negative slope of $m = -1.1^{+0.8}_{-0.6}$.

This negative relation between CO line ratios and metallicity has been reported before (e.g., J. Lequeux et al. 1994; A. A. Kepley et al. 2016; C. Cicone et al. 2017) and can be linked generally to the radial trend (see, radial metallicity trends) and, in the broader context, to the negative correlation we find with the galaxy-integrated M_* (see Figure 4) given the mass–metallicity relation (e.g., C. A. Tremonti et al. 2004). At lower metallicities, the environment will also exhibit lower dust-to-gas ratios (A. K. Leroy et al. 2011; V. Casasola et al. 2020) and hence

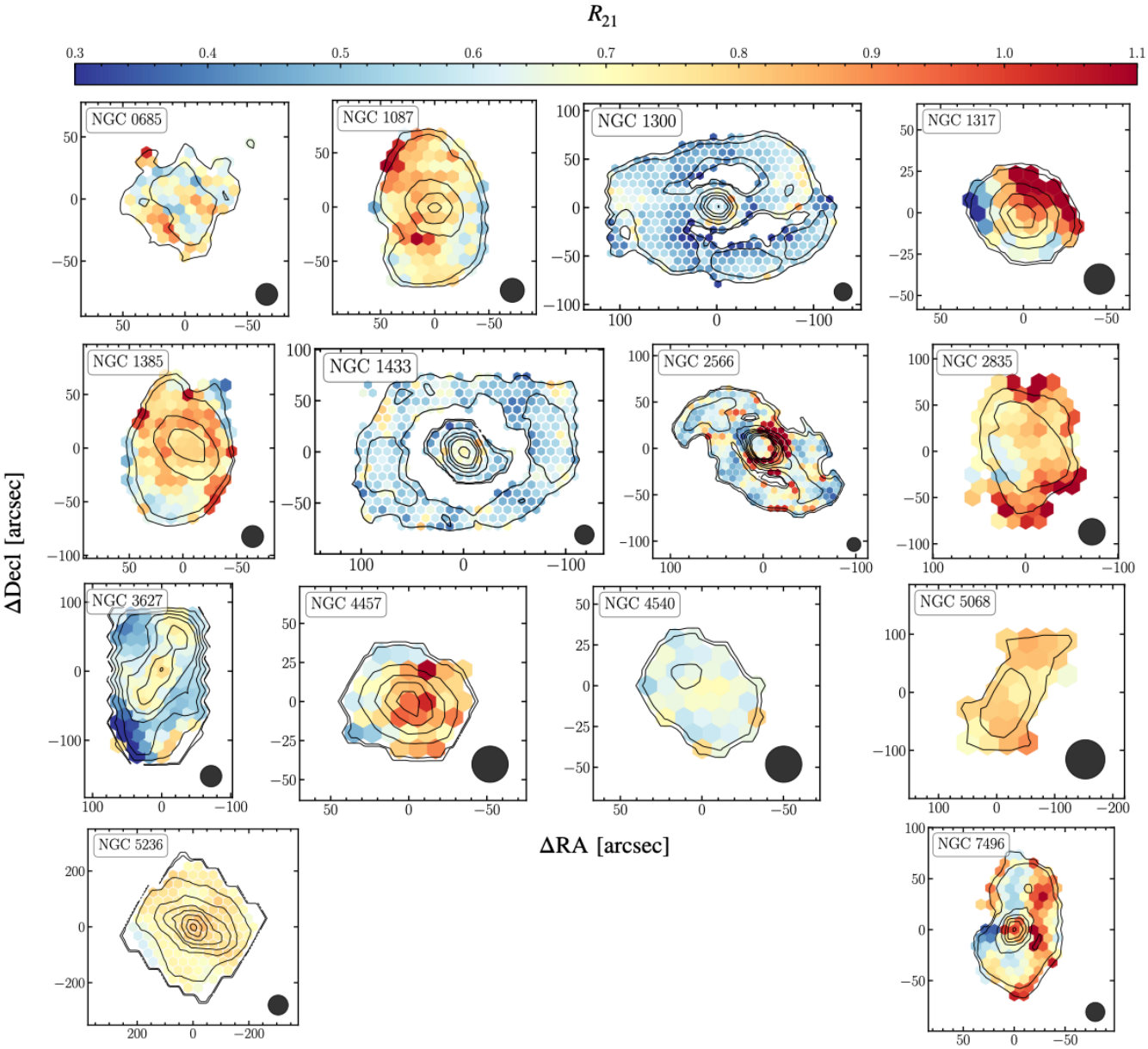

Figure 7. Resolved R_{21} variation. All maps have been convolved to a common physical resolution of 1.7 kpc. Only sight lines for which both the CO(1–0) and CO(2–1) emission are significantly detected at S/N > 5 are shown. The black circle in the bottom-right corner of each panel presents the beam. For reference, we illustrate the CO(1–0) integrated intensities using the black contour lines. These are drawn at 0.5, 1, 5, 10, 15, 20, 30, 40, and 50 K km s^{-1}.

less shielding and harder radiation fields probably driving both, more abundant and stronger excitation.

4.2. Variation of R_{21} within Individual Galaxies

We also investigate how the line ratio varies within the individual galaxies of our sample. Figure 7 illustrates the resolved R_{21} measurements per galaxy at 1.7 kpc physical resolution. From a qualitative inspection alone, it is evident that the line ratio clearly varies within the galaxies. For instance, five out of 14 sources show a clear increase of the line ratio toward the center (e.g., NGC 1300, NGC 1433, NGC 3627, NGC 4457, and NGC 7496) upon visual inspection.

Galactocentric radius—In Figure 8, we present the radial trends of the line ratio for each galaxy in our sample. Each panel also presents the stacked line ratio trend by stacking together all sight lines per bin irrespective of their S/N. For reference, we also plot the stacked line trends all together in a single panel in the bottom right. Here, we use the spectral stacking technique to quantify the radial trends. We show only stacked points where both stacked CO lines are significantly detected (S/N > 5).

Looking at the stacked trends, we note that five out of 14 galaxies show radial variations in terms of difference of the median line ratio for center and disk, which we report in Table 2. NGC 1300, NGC 1433, NGC 2566, and NGC 7496 show a clear increase toward the center with a flat trend of R_{21} across the disk. NGC 3627, in contrast, shows a continuous decreasing trend of R_{21} with galactocentric radius. Overall, the centers show a range of variation, which argues against a simple picture of more radiation leading to stronger excitation in centers. Likely, the presence of bars and the degree of turbulence play a critical role. To investigate this, however,

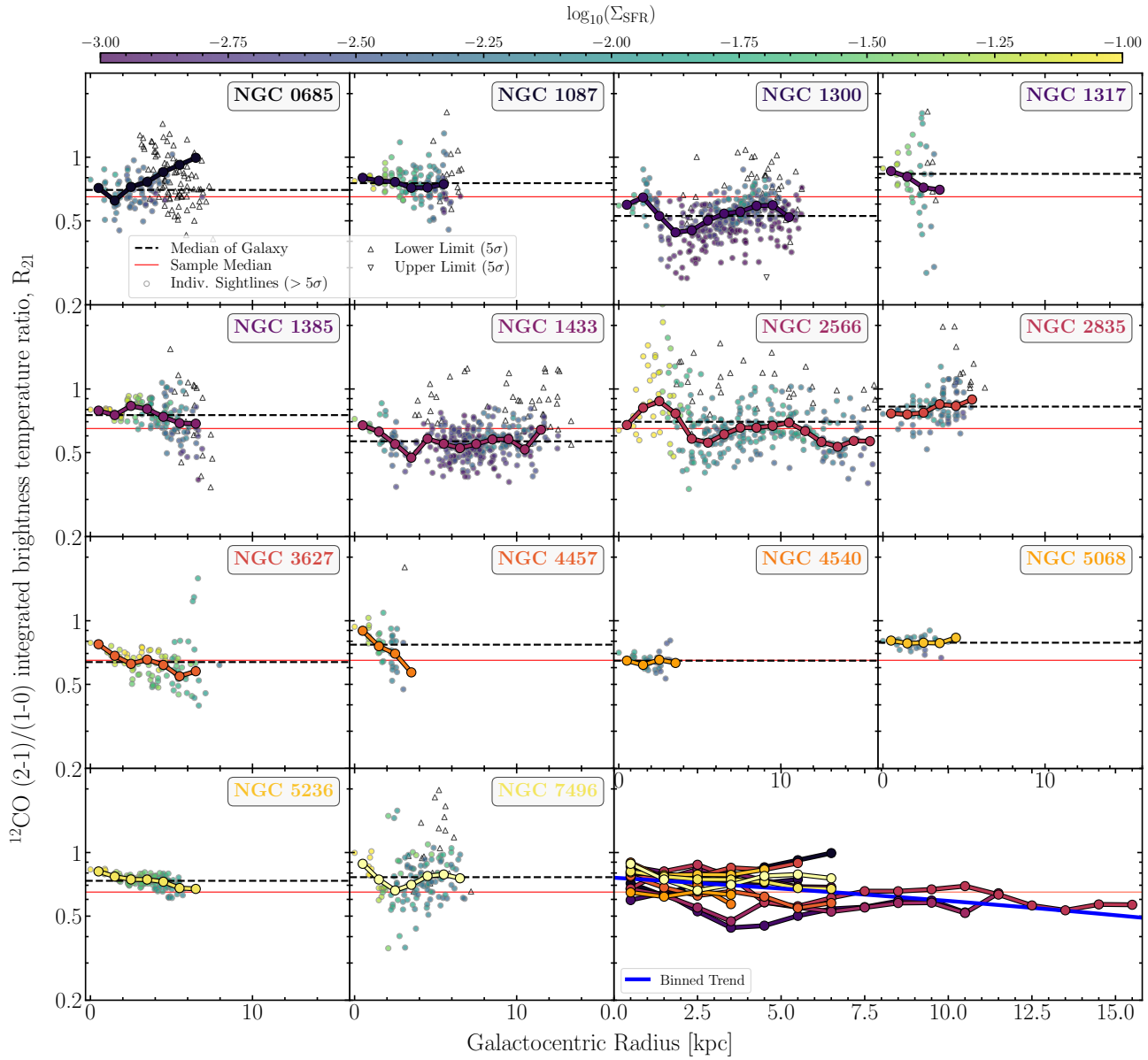

Figure 8. Radial R_{21} variation. The colored points represent significantly detected (S/N > 5) individual sight lines with adjacent lines of sight spaced by one half the beamwidth. Data with lower signal to noise are plotted using triangles either as upper or lower limits, if only one of the two CO transitions is significantly detected. The galaxy-wide median value for each individual galaxy is plotted as a dashed horizontal line. For reference, we plot all of the individual binned line trends in the bottom-right panel. The red dashed line represents the sample-wide CO line ratio median.

higher angular resolution are necessary that resolve scales where we can study the gas dynamics and kinematics. At larger radii, we include a larger amount of low-S/N data in our stack. Consequently, we are cautious about drawing overly definitive conclusions. Obtaining sensitive multiline observations of outer disks will provide valuable insights into whether there is a substantial change in CO excitation in the outer regions of disk galaxies.

SFR surface density—In Figure 9, we investigate the correlation of the CO line ratio with the SFR surface density per galaxy. Again, we use spectral stacking to quantify the overall trends. Previous studies suggest a relation of the CO ratio with SFR surface density. This is because higher SFR surface densities trace regions of higher-density gas (A. Usero et al. 2015; M. J. Gallagher et al. 2018), stronger radiation fields due to young stars present shortly after star formation (D. Narayanan & M. R. Krumholz 2014), and higher cosmic-ray densities. In our previous analysis when looking at all sight lines combined, we measured a positive correlation, with a slope of ∼0.1 for the binned medians (see Figure 6). For galaxies for which we have more than four independently stacked CO line ratio measurements, we repeat the measurement and perform a linear regression in the form of a power law to the stacked data points. We report the resulting slope in each panel.

We find a large range in slopes for the CO line ratio trends with SFR surface density. Some of the galaxies in our sample do not show any or only a mild correlation between the two quantities. For instance, NGC 1087, NGC 1300, NGC 1385, NGC 1433, and NGC 7496 all show slopes that are <0.05. When we perform a liner regression when combining all of the stacked trends, we get a slope of $m = 0.06$, which is shallower than the trend found when looking at the individual lines of sight. Overall, however, our results confirm that internal

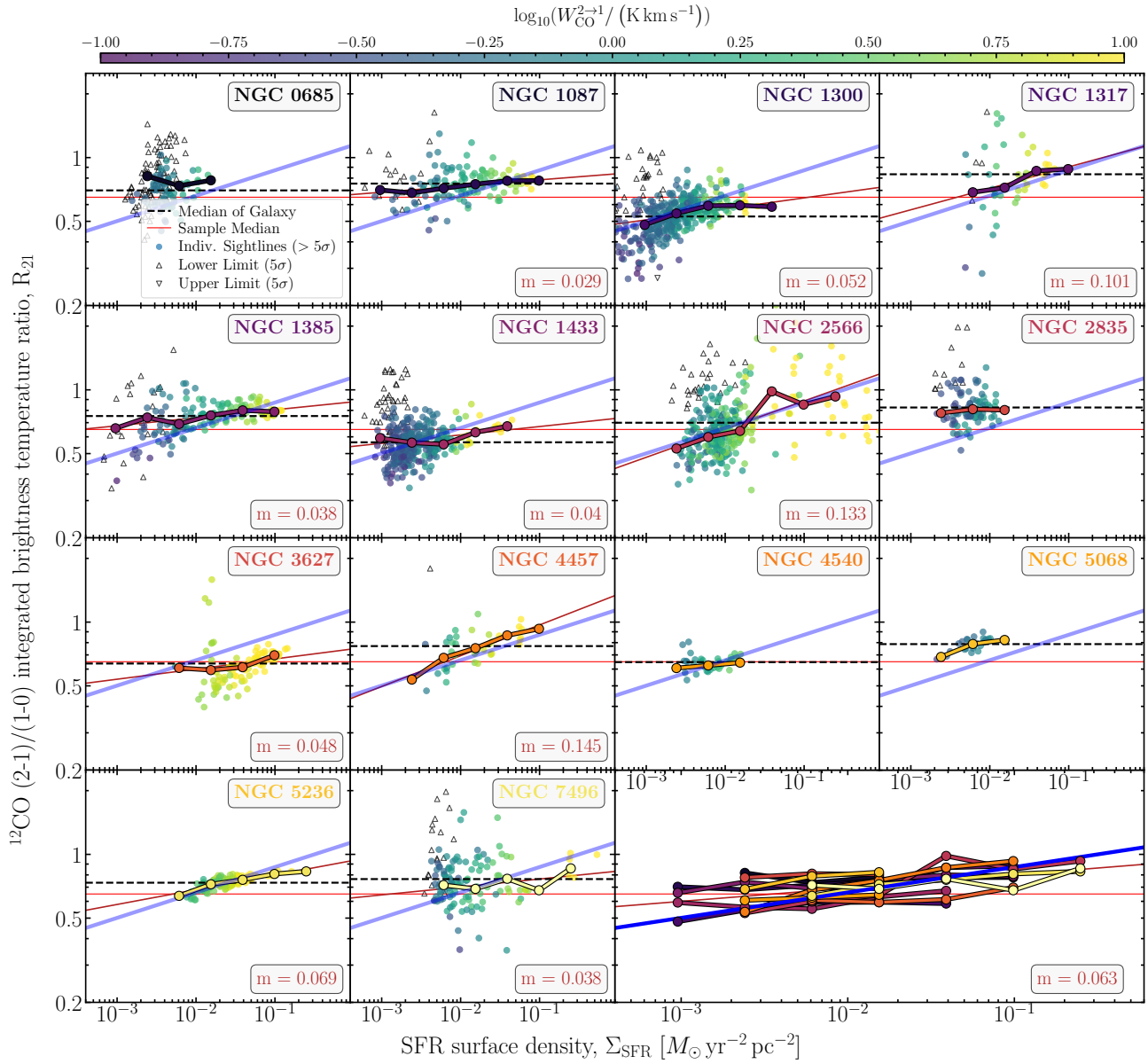

Figure 9. R_{21} variation with SFR surface density. This figure follows the layout and design of Figure 8. Here, the significantly detected sight lines are colored by their corresponding CO(2–1) integrated brightness temperature. In case more than four stacked points are available, we also report the slope of the power-law regression fitted to the stacked trend.

correlations exist between star formation activity and CO excitation in nearby, normal, star-forming galaxies. Nevertheless, to provide a more comprehensive conclusion, a larger sample of the galaxy population and at higher angular resolutions (to ensure resolving individual environments) will be necessary to explore potential variations across different environments.

4.3. Scatter of the Line Ratio

For a number of galaxies, we have CO(1–0) and/or CO(2–1) observations from different mapping surveys. Therefore, we can attempt to quantify instrumental-dependent scatter and systematic variation in the R_{21} line ratio value distribution by systematically assessing the different permutations of surveys to compute the line ratio. In Figure 10, we present the distribution of line ratio values per sight line for different combinations of surveys. For eight galaxies, we have CO(1–0) and CO(2–1) mapping coverage from multiple surveys. The left panel in Figure 10 shows the area-weighted average and 16th–84th percentile range for the different survey permutations per galaxy. For this comparison, we convolved all different CO(1–0) and CO(2–1) maps to the same resolution and only include sight lines per galaxy where we detect ($>5\sigma$) CO emission in all surveys. In the right panel of Figure 10, we quantify the change (in terms of absolute difference in mean R_{21}) for a given substitution of the survey. For reference, we list the means and 16th–84th percentile range of the line ratio distributions for the different survey permutations in Table 4.

From the left panel of Figure 10, it is evident that the average can systematically differ by up to 0.3 dex for the different permutations. For instance, for NGC 3627, the

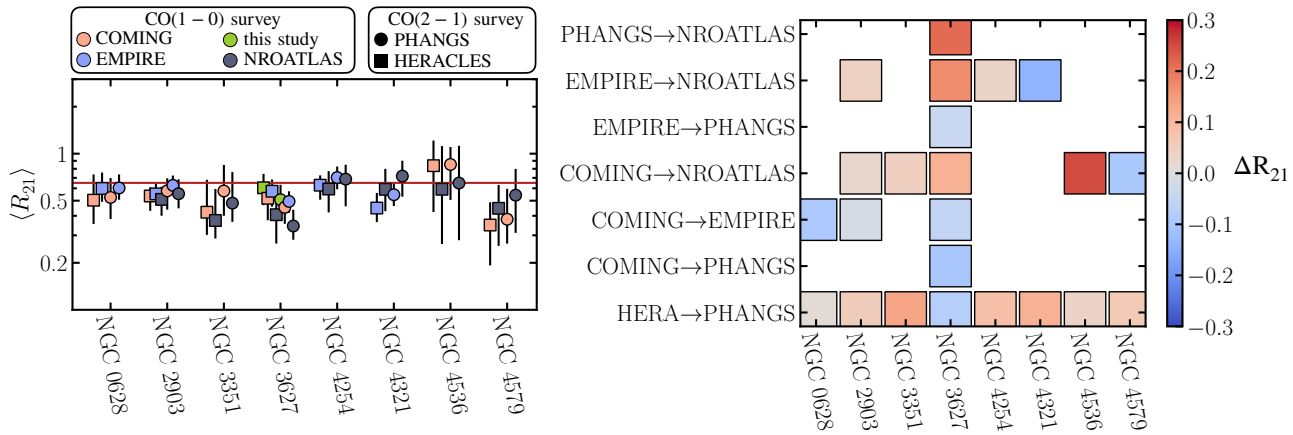

Figure 10. Estimating instrumental-dependent scatter in R_{21}. For a number of galaxies, we have CO(1–0) and/or CO(2–1) maps from different surveys, enabling up to eight permutations of CO line ratios (e.g., for NGC 3627). To estimate the scatter, we compare the R_{21} distribution using different permutations of CO(1–0) and CO(2–1) to compute the line ratio. Left panel: the (volume-weighted) mean and 16th–84th percentile range. Square markers indicate that CO(2–1) from HERACLES (A. K. Leroy et al. 2009) was used, and circle markers indicate that CO(2–1) from PHANGS (A. K. Leroy et al. 2021a) was used. The color of the marker indicates which CO(1–0) data set is used. The horizontal red line illustrates the galaxy-wide R_{21} average derived in this study. Right panel: the absolute change in the average R_{21} value based on substituting either the CO(1–0) or CO(2–1) data by a different survey, as indicated on the *y*-axis.

Table 4
Summary of Volume-weighted Average Line Ratio for Different Permutations

CO(2–1) Survey	PHANGS				HERACLES			
CO(1–0) Survey	COMING	ALMA	EMPIRE	NROATLAS	COMING	ALMA	EMPIRE	NROATLAS
NGC 0628	$0.50^{+0.22}_{-0.14}$	…	$0.60^{+0.15}_{-0.10}$	…	$0.52^{+0.16}_{-0.14}$	…	$0.60^{+0.12}_{-0.09}$	…
NGC 2903	$0.54^{+0.06}_{-0.10}$	…	$0.55^{+0.09}_{-0.04}$	$0.51^{+0.10}_{-0.10}$	$0.58^{+0.11}_{-0.13}$	…	$0.63^{+0.09}_{-0.07}$	$0.55^{+0.12}_{-0.10}$
NGC 3351	$0.42^{+0.25}_{-0.12}$	…	…	$0.37^{+0.21}_{-0.08}$	$0.58^{+0.26}_{-0.17}$	…	…	$0.48^{+0.27}_{-0.11}$
NGC 3627	$0.52^{+0.09}_{-0.14}$	$0.60^{+0.13}_{-0.13}$	$0.57^{+0.10}_{-0.11}$	$0.41^{+0.11}_{-0.14}$	$0.45^{+0.05}_{-0.09}$	$0.51^{+0.12}_{-0.06}$	$0.49^{+0.07}_{-0.07}$	$0.34^{+0.09}_{-0.06}$
NGC 4254	…	…	$0.63^{+0.09}_{-0.11}$	$0.59^{+0.17}_{-0.17}$	…	…	$0.70^{+0.11}_{-0.10}$	$0.69^{+0.15}_{-0.22}$
NGC 4321	…	…	$0.45^{+0.10}_{-0.08}$	$0.59^{+0.20}_{-0.16}$	…	…	$0.55^{+0.09}_{-0.08}$	$0.72^{+0.17}_{-0.18}$
NGC 4536	$0.84^{+0.36}_{-0.41}$	…	…	$0.59^{+0.51}_{-0.32}$	$0.85^{+0.23}_{-0.34}$	…	…	$0.65^{+0.46}_{-0.36}$
NGC 4579	$0.35^{+0.13}_{-0.15}$	…	…	$0.45^{+0.17}_{-0.19}$	$0.38^{+0.21}_{-0.11}$	…	…	$0.54^{+0.24}_{-0.23}$

Note. The table lists the median and 16th–84th percentile range.

equally weighted average ranges from $0.34^{+0.09}_{-0.06}$ when using CO(1–0) from NROATLAS and CO(2–1) from HERACLES to $0.60^{+0.13}_{-0.13}$ when using ALMA CO(1–0) and CO(2–1) observations.[23] Looking at the right panel in Figure 10, there seem to be systematic changes when substituting different surveys. For instance, when substituting the CO(2–1) observations from the HERACLES survey with the data from the PHANGS survey, the resulting R_{21} is consistently larger by an absolute value of ∼0.1, apart for NGC 3627. The overall systematic offsets in the average line ratio of 10%–20% are expected within the uncertainty of flux calibration.

We note that this telescope-dependent variation is on a similar magnitude (i.e., 10%–20%) to the overall dynamical range we find for the line ratio. We emphasize again that in this analysis, we account for the instrumental variation, which does not contribute to the scatter observed within each individual galaxy. We also note that the line ratio average variation can, to a certain degree, result from the different sensitivity of various surveys. In our cross-sample comparison, however, we ensured to use sight lines that have a detection in all surveys, therefore limiting such bias (but we note that this leads to a bias to the more CO luminous sight lines). The finding of the scatter within each galaxy being greater than the galaxy-to-galaxy variation supports the same conclusion that the scatter within a galaxy (∼0.1–0.2 dex) is more significant than the galaxy-to-galaxy scatter (∼0.05 dex). Such galaxy-internal variation is mostly driven by different environments, e.g., center, bars, and the contrast between spiral arm and interarm.

[23] We note, however, that NGC 3627 was an HERACLES pilot study. The observations were of lower quality, which can partially explain the large variation with other observations of NGC 3627.

4.4. Comparison to Other Surveys

Numerous mapping surveys that combine CO(1–0) and CO(2–1) at kiloparsec scales to investigate R_{21} across nearby galaxies exist (A. K. Leroy et al. 2013; J. S. den Brok et al. 2021; Y. Yajima et al. 2021; A. K. Leroy et al. 2022). An overview of the various galaxies and the particular mapping surveys that covered them can be found in Table 5. However, so far, these mapping surveys are based on single-dish observations, mostly using the either the IRAM 30 m or the Nobeyama 45 m telescope. Aggregated over the whole sample and combining the single-dish surveys, a consistent galaxy-wide R_{21} average of around 0.65 is found. In Figure 11, we compare the galaxy-integrated line ratio measurements of this sample to

Table 5
Overview of which CO(1–0) and CO(2–1) Mapping Surveys Cover which Galaxies from All Available Surveys

	CO(1–0)				CO(2–1)	
Galaxy	ALMA (cycle 9)	EMPIRE	COMING	NROATLAS	HERACLES	PHANGS
NGC 0253	✗	✗	✗	✓	✗	✓
NGC 0337	✗	✗	✓	✗	✓	✗
NGC 0628	✗	✓	✓	✗	✓	✓
NGC 0685	✓	✗	✗	✗	✗	✓
NGC 1068	✗	✗	✗	✓	✗	✓
NGC 1087	✓	✗	✓	✗	✗	✓
NGC 1300	✓	✗	✗	✗	✗	✓
NGC 1317	✓	✗	✗	✗	✗	✓
NGC 1385	✓	✗	✗	✗	✗	✓
NGC 1433	✓	✗	✗	✗	✗	✓
NGC 2146	✗	✗	✓	✗	✓	✗
NGC 2566	✓	✗	✗	✗	✗	✓
NGC 2775	✗	✗	✓	✗	✗	✓
NGC 2835	✓	✗	✗	✗	✗	✓
NGC 2841	✗	✗	✓	✗	✓	✗
NGC 2903	✗	✓	✓	✓	✓	✓
NGC 2976	✗	✗	✓	✗	✓	✗
NGC 3077	✗	✗	✓	✗	✓	✗
NGC 3147	✗	✗	✓	✗	✓	✗
NGC 3184	✗	✓	✗	✓	✓	✗
NGC 3198	✗	✗	✓	✗	✓	✗
NGC 3351	✗	✗	✓	✓	✓	✓
NGC 3521	✗	✗	✓	✗	✓	✓
NGC 3627	✓	✓	✓	✓	✓	✓
NGC 3631	✗	✗	✗	✗	✓	✗
NGC 3938	✗	✗	✓	✗	✓	✗
NGC 4030	✗	✗	✓	✗	✓	✗
NGC 4051	✗	✗	✗	✗	✓	✗
NGC 4214	✗	✗	✓	✗	✓	✗
NGC 4254	✗	✓	✗	✓	✓	✓
NGC 4303	✗	✗	✓	✗	✓	✓
NGC 4321	✗	✓	✗	✓	✓	✓
NGC 4457	✓	✗	✗	✗	✗	✓
NGC 4535	✗	✗	✗	✗	✓	✓
NGC 4536	✗	✗	✓	✓	✓	✓
NGC 4540	✓	✗	✗	✗	✗	✓
NGC 4548	✗	✗	✗	✗	✓	✓
NGC 4569	✗	✗	✗	✓	✓	✓
NGC 4579	✗	✗	✓	✓	✓	✓
NGC 4654	✗	✗	✗	✗	✓	✓
NGC 4666	✗	✗	✓	✗	✓	✗
NGC 4689	✗	✗	✗	✗	✓	✓
NGC 4736	✗	✗	✗	✓	✓	✗
NGC 5055	✗	✓	✓	✓	✓	✗
NGC 5068	✓	✗	✗	✗	✗	✓
NGC 5194	✗	✓	✗	✗	✓	✗
NGC 5236	✓	✗	✗	✗	✗	✓
NGC 5248	✗	✗	✓	✗	✓	✓
NGC 5364	✗	✗	✓	✗	✓	✗
NGC 5457	✗	✗	✗	✓	✓	✗
NGC 5713	✗	✗	✓	✗	✓	✗
NGC 6946	✗	✓	✗	✓	✓	✗
NGC 7331	✗	✗	✓	✗	✓	✗
NGC 7496	✓	✗	✗	✗	✗	✓

the ones presented in J. S. den Brok et al. (2021; who found a CO(1–0) intensity-weighted average of $\langle R_{21} \rangle = 0.64 \pm 0.09$) and A. K. Leroy et al. (2022; who reported $\langle R_{21} \rangle = 0.65^{+0.18}_{-0.15}$). In particular, the sample of galaxies covered in A. K. Leroy et al. (2022), which spans a comparable range in total SFR and stellar mass to the survey in this study, exhibits a large galaxy-to-galaxy scatter (of around 0.3 dex). We find that the average ratios across our galaxy sample are consistent—within the scatter—with the median value found by R. P. Keenan et al. (2024), who conducted unresolved, single-pointing, single-dish observations. Their study, which spans 122 galaxies, reports a median ratio of $\langle R_{21} \rangle = 0.71^{+0.25}_{-0.20}$. The slightly higher ratio of 0.71 compared to our value of 0.64 may be attributed to the fact that their single-pointing observations are biased toward the

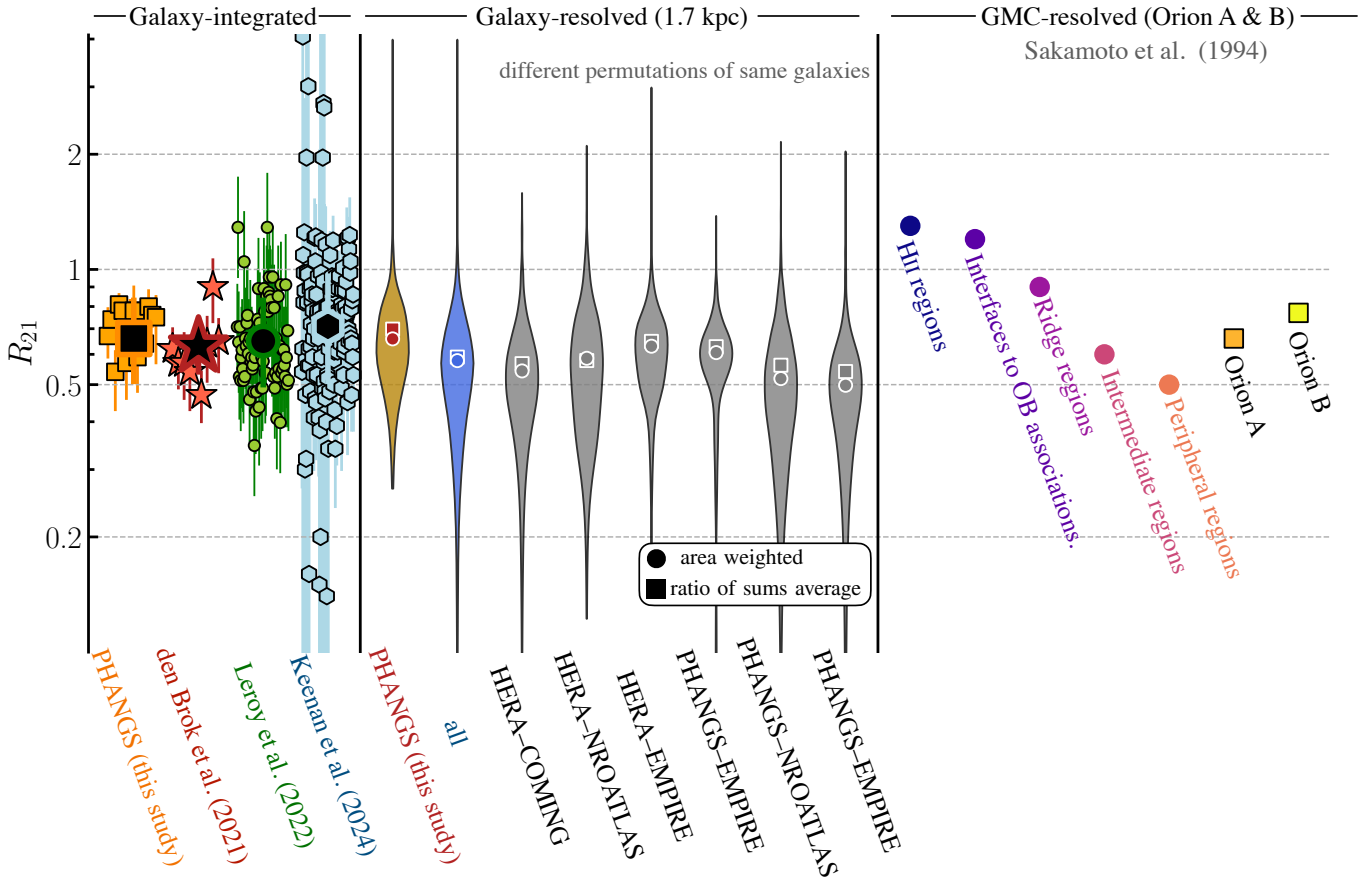

Figure 11. Comparing R_{21} ratio surveys at different scales. Galaxy integrated: each marker represents the median line ratio per galaxy. We also illustrate the sample-wide median and 16th–84th percentile range using a larger, gray-colored marker. The *y*-axis carries no information. The markers are slightly offset along the *y*-axis, such that points are individually recognizable. Galaxy resolved: histogram of sight line R_{21} value distribution for different permutations of surveys. The volume- and intensity-weighted averages are represented with a circle or square, respectively, for each distribution. The dark-orange distribution is using the data presented in this study. The blue distribution is combining all data from all surveys. The gray distributions represent the results using a different survey for CO(2–1) (first name in the *x*-axis) and CO(1–0) (second name). The dotted line represents the average value derived by this study. GMC-resolved: for reference, the panel also presents the reported average value for GMC-resolved observations using the Orion A and B clouds as reference. The values are adopted from S. Sakamoto et al. (1994).

brighter central regions (as the pointings are centered on the galaxy centers and might not include the full outskirts of the galaxy depending on its apparent size).

For reference, we also reported the average line ratio values derived from GMC-resolved observations (S. Sakamoto et al. 1994) in Figure 11. For the Orion A cloud, a value of 0.66 is reported, while Orion B, on average, measures a ratio of 0.71. Within the cloud, the value of R_{21} is observed to increase to above unity toward H II and OB association regions. While Orion A & B are likely not representative of the entire extragalactic GMC population, these values still indicate that the average line ratios we observe within galaxies are mostly dominated by the intermediate and perioheral regions of GMCs.

We also present a more detailed comparison when combining samples of single-dish observations in Figure 11. The central part of the figure illustrates the line-of-sight R_{21} value distribution across the sample of galaxies using different combinations of CO(1–0) and CO(2–1) maps (see Table 5). We notice that in particular when using the Nobeyama 45 m CO(1–0) observations to derive R_{21}, the galaxy-wide average seems to be systematically lower by ∼0.1 dex. Based on this panel and the observed offset alone, it is not clear if this is a selection effect, since the R_{21} distributions are not necessarily drawn from the same galaxies or even same field of view, as different surveys mapped different galaxies. In Figure 12, we additionally compare the relation of R_{21} as function of the SFR surface using all sight lines from the sample observed in this study (presented in red) with the single-dish-based result presented in A. K. Leroy et al. (2022; presented in black) and the correlation reported by R. P. Keenan et al. (2025) for galaxy-integrated measurements (blue line). Two things are evident: (i) the scatter when only using ALMA CO(1–0) and CO(2–1) data is lower (despite a similar dynamical range of the galaxies' SFR and stellar mass in the sample), but (ii) the relation of R_{21} and SFR surface density shows a similar slope of around 0.1, despite the difference in the scatter for all three studies.

This comparison underscores that SFR surface density serves as a predictor for R_{21} variation, in agreement with previous studies. While there is some scatter, approximately 0.5 dex, around the correlation for a given SFR, this relationship remains the most robust method currently available for predicting R_{21} across diverse galactic environments, especially within the SFR surface density range[24] of 10^{-3}–$10^{0}\,M_{\odot}\,\mathrm{yr}^{-1}\,\mathrm{kpc}^{-2}$.

[24] We have employed a single power law given our limited dynamical range. We expect the trend to flatten at both high $\Sigma_{\rm SFR}$ (toward unity at $\Sigma_{\rm SFR} \gtrsim 0.3\,M_{\odot}\,\mathrm{yr}^{-1}\,\mathrm{kpc}^{-2}$) and low $\Sigma_{\rm SFR}$ (the ratio will likely not go below ∼0.3). Therefore, it is feasible to establish more complex fitting relations (see, e.g., A. K. Leroy et al. 2022; R. P. Keenan et al. 2024, who use a broken power-law fit with a flat trend above and below some threshold values). However, in our case, we do not include such a fit, given the limited dynamic range.

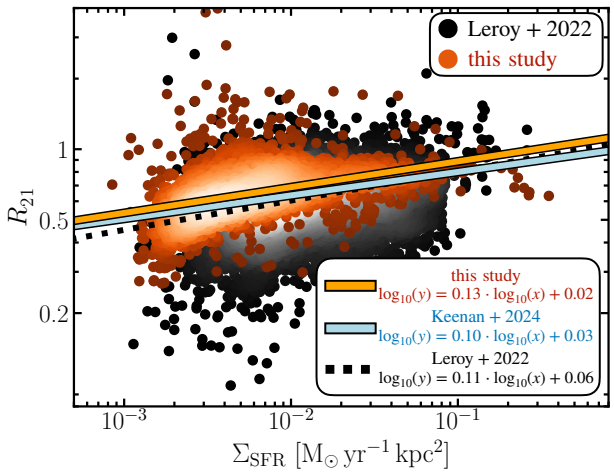

Figure 12. R_{21} literature sight-line comparison. The points show the correlation of the line ratio to the SFR surface density. The dark-orange points indicate the data from this study, and the black points are from A. K. Leroy et al. (2022). The red solid line is a linear regression fit (in log–log space) through the individually detected sight lines. The blue line presents the fit reported by R. P. Keenan et al. (2025), and the black dotted line represents the fit derived by A. K. Leroy et al. (2022).

Investigating the factors contributing to this scatter offers a promising direction for future research.

5. Discussion

5.1. Impact on Resolved Molecular Gas Scaling Relations

There is broad interest in the rate at which stars form from molecular gas in galaxies and how this rate varies as a function of host galaxy and local environment (e.g., J. S. Young & N. Z. Scoville 1991; J. S. Young et al. 1996; R. C. Kennicutt & N. J. Evans 2012). One point motivating the study of R_{21} has been to understand how the CO line used for a particular study impacts results on this topic.

There are several formalisms adopted to study variations in SFR per unit molecular mass. This quantity is often expressed as the star formation efficiency of H_2 (e.g., J. S. Young et al. 1996; A. K. Leroy et al. 2008) or the molecular gas depletion time (e.g., A. Saintonge & B. Catinella 2022),

$$\tau_{\rm dep}^{\rm mol} = \frac{\Sigma_{\rm mol}}{\Sigma_{\rm SFR}} \tag{2}$$

which captures the time that it would take star formation to consume the available molecular gas reservoir. One of the most popular framings has been to assume that the molecular gas surface density represents a controlling parameter and to study the Kennicutt–Schmidt (K–S) relation (M. Schmidt 1959; R. C. Kennicutt 1998) in its molecular form,

$$\frac{\Sigma_{\rm SFR}}{M_\odot\ {\rm yr}^{-1}\,{\rm kpc}^{-2}} = c \times \left(\frac{\Sigma_{\rm mol}}{M_\odot\ {\rm pc}^{-2}}\right)^N. \tag{3}$$

Use of the molecular form of the K–S relation reflects that molecular gas is the phase observed to correlate most directly with tracers of star formation at ≈kpc scales (T. Wong & L. Blitz 2002; F. Bigiel et al. 2008; A. Schruba et al. 2011). The parameter c describes an amplitude related to the star formation efficiency and gas depletion time, and the variation of SFR per unit gas as a function of $\Sigma_{\rm mol}$ is captured by the power-law index, N (hereafter refereed to as the K–S index). Though focusing exclusively on N misses the dependence of the SFR per molecular gas on any environmental factor other than $\Sigma_{\rm mol}$, N has become a popular, if imperfect, shorthand for the influence of environment on the star formation process.

In Figure 13, we compare the K–S relation for the two transitions and report differences in the best-fit K–S index N for the two transitions. In these plots, we use a radially varying CO-to-H_2 conversion factor based on the prescription from A. D. Bolatto et al. (2013) and computed for the galaxies in our sample by J. Sun et al. (2022). However, these value do not account for variations in the line ratio (e.g., E. Schinnerer & A. K. Leroy 2024, where this term is considered). We find K–S indices ranging from $N = 0.5$ to 1.12, though we note that the adopted fitting technique, as well how upper limits are treated, impacts the precise K–S index derivation (e.g., A. K. Leroy et al. 2013). To compare results for the two transitions, we fit the relation to the same points when using the CO(2–1) measurements and a fixed R_{21}. We note that the derived K–S indices should only be compared cautiously with literature results, as the measurements are sensitive to the specific methodology used for calculating the slopes.

Figure 13 shows that for most galaxies, the choice of line has a modest impact on the estimated N. When combining all sight lines across all galaxies, the K–S index only changes by -2%, from $N_{10} = 0.80$ to $N_{21} = 0.78$. The impact on individual galaxies is larger but still usually modest. For 10 out of 14 targets, N varies by <0.1 or $\pm 10\%$ between CO(1–0) and CO(2–1). For seven of these targets, the change in the K–S index is $<5\%$. The other four galaxies that show more significant variations are NGC 1317, NGC 2835, NGC 3627, and NGC 5068. For 11/14 galaxies, the K–S index decreases when using CO(2–1) instead of CO(1–0). This is expected, as we find elevated R_{21} values at larger SFR surface densities (see Figure 9). As a result, the assumption of a fixed line ratio will lead to overestimating the CO(2–1) derived molecular gas mass surface densities at larger SFR surface densities, which will flatten the K–S relation and lead to lower K–S index. The sense of our results is consistent with similar discussions in Y. Yajima et al. (2021) and A. K. Leroy et al. (2022), though we find smaller overall impact of line choice on N. See J. Sun et al. (2023) for a recent study of the impact of a variety different SFR and $\alpha_{\rm CO}$ prescriptions on N in the PHANGS–ALMA data set, also at kiloparsec-scale resolution.

In Figure 14, we show the effect of line choice on the estimated $\tau_{\rm dep}^{\rm mol}$ (Equation (2)) for whole galaxies and for only galaxy centers. Formally, we find that for eight of 14 galaxies, the distribution of depletion times across the whole disk differ significantly between the two lines when assuming a fixed R_{21}. However, the figure also shows that the variations of $\tau_{\rm dep}^{\rm mol}$ from galaxy to galaxy and from galaxy center to galaxy centers are mostly not a result of line choice. For the most part, these appear similar regardless of line choice. That is, a galaxy seen to have high $\tau_{\rm dep}^{\rm mol}$ using CO (1–0) also shows high $\tau_{\rm dep}^{\rm mol}$ using CO (2–1).

Figures 13 and 14 therefore suggest that the impact of R_{21} variation on the derived scaling relations is minimal for kiloparsec-scale observations of main-sequence galaxies. For individual galaxies, the bias induced by assuming using CO(2–1) and a fixed R_{21} does generally not exceed 10%. This is smaller than uncertainties in the CO-to-H_2 conversion

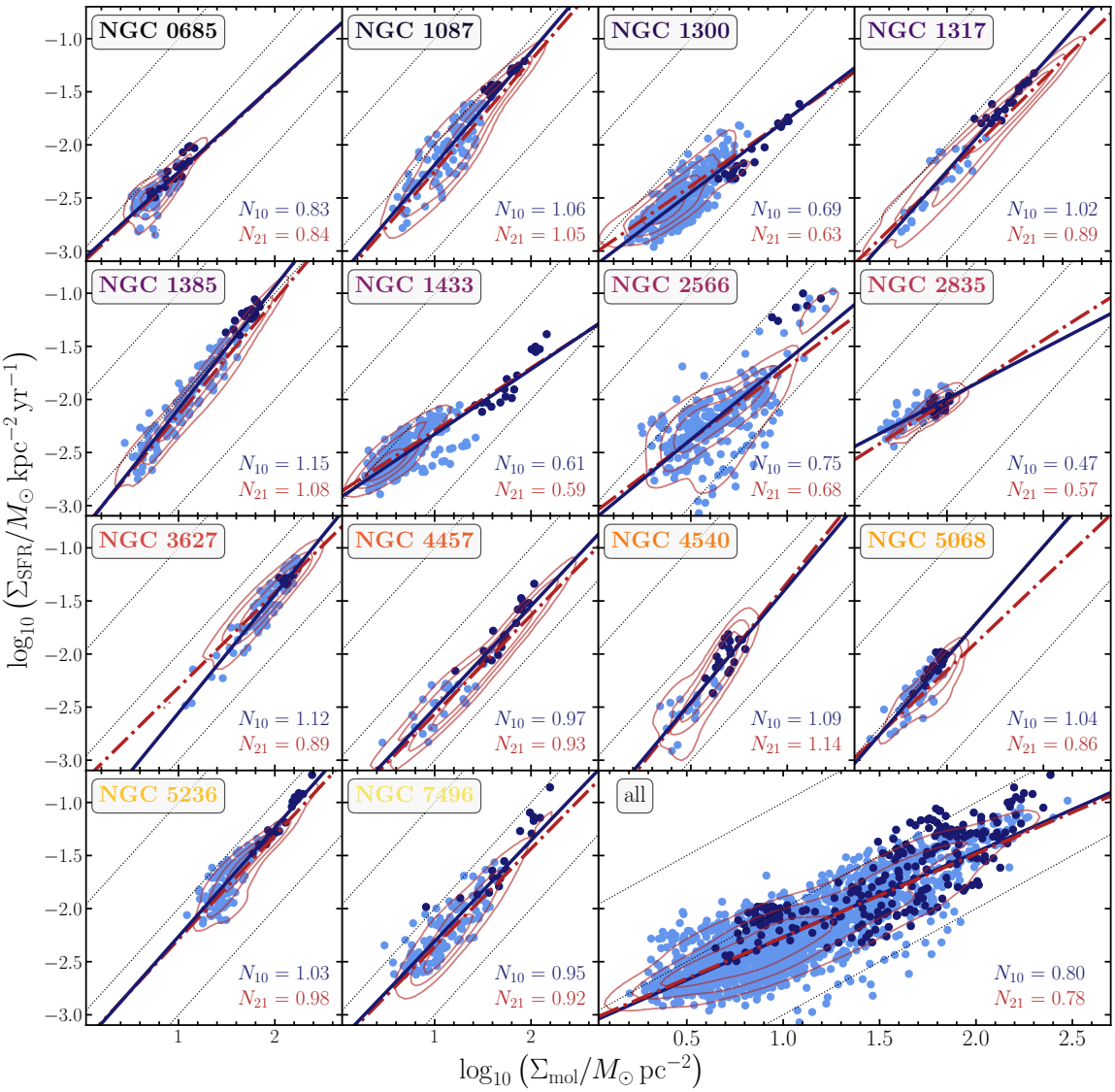

Figure 13. The Kennicutt–Schmidt (K–S) relation. The blue points show the correlation of the molecular gas surface density based on the CO(1–0) line intensity with SFR surface density. The dark-blue points indicate central ($r < 2$ kpc) sight lines. We fit a linear regression in log–log space and report the slope, which corresponds to the K–S index, in each panel (N_{10}). The red contours show the distribution of the same sight lines but using the CO(2–1) and a fixed $R_{21} = 0.64$ to determine the molecular gas surface density. The red dashed line shows the linear regression to the CO(2–1)-based points. The corresponding K–S index, N_{21}, is indicated in each panel as well. The diagonal dotted lines indicate constant depletion time of 0.1, 1, and 10 Gyr from top to bottom.

factor, especially for galaxy centers (K. M. Sandstrom et al. 2013; J. S. den Brok et al. 2023a; Y.-H. Teng et al. 2023). Despite their modest magnitude, as we have seen above, physical variations in the line ratio do exist and should be accounted for to achieve the best estimates of N and $\tau_{\rm dep}^{\rm mol}$.

5.2. How to Predict R_{21} at Kiloparsec Scales?

Overall, assuming a fixed $R_{21} = 0.64$—for either the galaxy-wide average or for kiloparsec-sclae sight lines—will not significantly bias the resulting molecular gas scaling relations for massive main-sequence galaxies if dealing with relations across a sample. For an improvement of accuracy, we suggest the following options:

(i) For unresolved galaxy observations, stellar mass serves as an effective predictor of variations in R_{21} (see the left panel of Figure 4). Our findings indicate that higher stellar mass galaxies tend to have lower R_{21} ratios. Therefore, if integrated stellar mass measurements are available, the galaxy-wide average ratio can be approximated using the following empirical relation (valid for the stellar mass range of $\sim 10^9$–$10^{11}\,M_\odot$):

$$\log_{10}\langle R_{21}\rangle_{\rm gal} \approx -0.07 \pm 0.02 \log_{10}\left(\frac{M_*^{\rm gal}}{M_\odot}\right) + 0.57 \pm 0.09. \quad (4)$$

Note that in particular for single-dish observations, the scatter is expected to be in the range of 0.1–0.2 dex due to additional flux calibration uncertainties. Therefore, we recommend using the fixed line ratio of $R_{21} = 0.64$ if flux calibration uncertainty is expected to be large (>10%).

(ii) In the context of resolved, kiloparsec-scale observations, the SFR surface density ($\Sigma_{\rm SFR}$) provides a robust predictor for R_{21}. Specifically, the relation indicates that regions with higher $\Sigma_{\rm SFR}$ tend to exhibit higher R_{21} ratios. Our study (see Table 3) suggests the following relationship for SFR surface densities

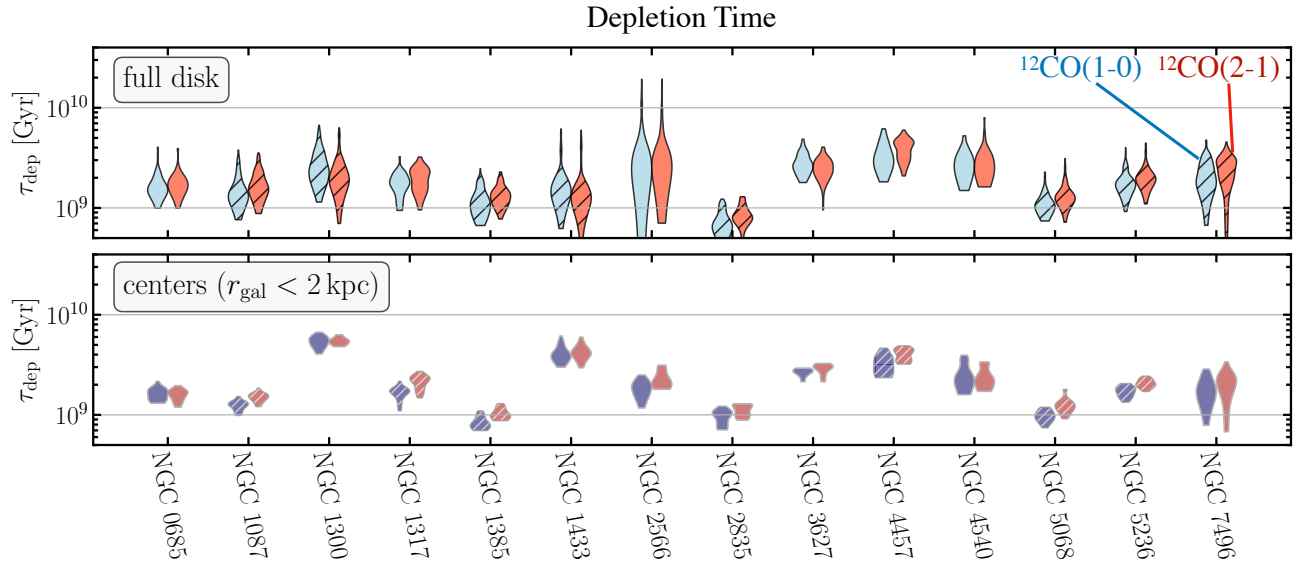

Figure 14. Galaxy-to-galaxy variation in depletion time. These panels contrast the bulk molecular gas depletion time using either the CO(1–0), in blue, or CO(2–1) and a fixed R_{21}, in red. The top panel presents the distribution across the full galaxy disks. The bottom panel illustrates the distribution for the central galaxy points ($r_{gal} < 2$ kpc). Where the distribution of depletion times when either using CO(1–0) or CO(2–1) differs significantly based on a K–S test, they are presented using hatched violins.

with R_{21} (valid for the SFR surface density range of $\sim 10^{-3}$–$10^{-1}\,M_\odot\,\mathrm{yr}^{-1}\,\mathrm{kpc}^{-2}$):

$$\log_{10} R_{21}^{1.7\,\mathrm{kpc}} \approx 0.12^{+0.03}_{-0.03} \log_{10}\left(\frac{\Sigma_{\mathrm{SFR}}}{M_\odot\,\mathrm{yr}^{-1}\,\mathrm{kpc}^{-2}}\right) + 0.06^{+0.07}_{-0.09}. \quad (5)$$

Note that a scatter of 0.1 dex can be expected, particularly when different galactic environments, such as the center and disk, are included. Future work will investigate whether combining both predictors—stellar mass and SFR surface density—might improve the accuracy for both scales in predicting R_{21}.

6. Conclusions

Here, we present new ALMA Morita ACA (7 m + TP) CO(1–0) maps of 12 nearby galaxies ($D_{gal} \lesssim 20$ Mpc). We combine this data set with two archival CO(1–0) maps and CO(2–1) ALMA data from the PHANGS–ALMA survey. We convolve all observations to a common physical resolution of 1.7 kpc, which corresponds to the smallest common scale. With the combined CO(1–0) and CO(2–1) data, we investigate R_{21} variation across and within the galaxies. In particular, we address the following science questions:

1. To what degrees do varying physical conditions in the gas, and uncertainties in the relative flux calibration, contribute to previously observed galaxy-to-galaxy scatter in R_{21}? We find an overall galaxy-to-galaxy scatter of 0.06 dex in the global average R_{21}, which is lower than the >0.1 dex reported by previous studies with comparable sample sizes. We conclude that previous single-dish surveys particularly suffered from flux calibration uncertainties of up to 20%, which significantly affected the measured galaxy-to-galaxy scatter.
2. On what magnitude does the CO line ratio R_{21} vary at 1.7 kpc physical resolution across the distinct environments of center, disk, arm, and interarm? We find a 0.1 dex internal variation in R_{21} within galaxies, which dominates over the 0.06 dex galaxy-to-galaxy scatter. At a physical resolution of 1.7 kpc, we observe an increase of R_{21} toward the center of the galaxies, where the mean value increases to 0.75 (15% increase).
3. How well can we parameterize the R_{21} variation (e.g., as a function of SFR surface density) across and within nearby galaxies? We investigate correlations of R_{21} with galactocentric radius, SFR surface density, specific SFR, and metallicity. We find significant correlations, as quantified by the Kendall's τ correlation coefficient, with all four parameters. The most significant correlation is found with the SFR surface density. In logarithmic space, we find a linear regression with a slope of 0.12 when fitting to the binned lines of sight, and 0.11 when fitting to all lines of sight. We note, however, that individual galaxies can show steeper or shallower correlations between the SFR surface density and R_{21}.

Overall, we find that using CO(2–1) and assuming a fixed R_{21} does not significantly bias molecular gas mass estimates at kiloparsec-scale resolution across large samples of galaxies. In contrast, systematic uncertainties in the flux calibration (particularly from single-dish telescope) and CO-to-H_2 conversion factor are more significant and can drive galaxy-to-galaxy scatter in molecular gas mass estimates as well as scatter within individual galaxies. We recommend an average $R_{21} = 0.64$, which is consistent with previous findings. We note, however, that when only looking into an individual galaxy, the induced bias by a fixed line ratio can be important, especially in regions close to the galaxy center. Expanding the sample beyond the massive star-forming galaxy population along with obtaining GMC-scale resolved observations will be fundamental in obtaining further constraints and insights into the environmental dependent variation of R_{21} in the ISM.

Acknowledgments

This work was carried out as part of the PHANGS collaboration. J.d.B. and E.W.K. acknowledge support from the Smithsonian Institution as a Submillimeter Array (SMA) Fellow. J.S. acknowledges support by the National Aeronautics and Space Administration (NASA) through the NASA Hubble Fellowship grant HST-HF2-51544 awarded by the Space Telescope Science Institute (STScI), which is operated by the Association of Universities for Research in Astronomy, Inc., under contract NAS 5-26555. H.A.P. acknowledges support from the National Science and Technology Council of Taiwan under grant 113-2112-M-032-014-MY3. A.K.L. gratefully acknowledge support from NSF AST AWD 2205628, JWST-GO-02107.009-A, and JWST-GO-03707.001-A and support by a Humbolt Research Award. F.H.L. acknowledges support from the Scatcherd European Scholarship of the University of Oxford. A.U. acknowledges support from the Spanish grant PID2022-138560NB-I00, funded by MCIN/AEI/10.13039/501100011033/FEDER, EU.

This paper makes use of the following ALMA data: ADS/JAO.ALMA#2012.1.00650.S, ADS/JAO.ALMA#2013.1.00803.S, ADS/JAO.ALMA#2013.1.01161.S, ADS/JAO.ALMA#2015.1.00121.S, ADS/JAO.ALMA#2015.1.00782.S, ADS/JAO.ALMA#2015.1.00925.S, ADS/JAO.ALMA#2015.1.00956.S, ADS/JAO.ALMA#2016.1.00386.S, ADS/JAO.ALMA#2017.1.00392.S, ADS/JAO.ALMA#2017.1.00766.S, ADS/JAO.ALMA#2017.1.00886.L, ADS/JAO.ALMA#2018.1.01321.S, ADS/JAO.ALMA#2018.1.01651.S, ADS/JAO.ALMA#2018.A.00062.S, ADS/JAO.ALMA#2019.1.01235.S, ADS/JAO.ALMA#2019.2.00129.S, ADS/JAO.ALMA#2022.1.01479.S, ADS/JAO.ALMA#2015.1.01538.S, ADS/JAO.ALMA#2017.1.00079.S,

ALMA is a partnership of ESO (representing its member states), NSF (USA), and NINS (Japan), together with NRC (Canada), NSC and ASIAA (Taiwan), and KASI (Republic of Korea), in cooperation with the Republic of Chile. The Joint ALMA Observatory is operated by ESO, AUI/NRAO, and NAOJ. The National Radio Astronomy Observatory is a facility of the National Science Foundation operated under cooperative agreement by Associated Universities, Inc.

Facility: ALMA.

Software: astropy (Astropy Collaboration et al. 2013, 2018, 2022), numpy (C. R. Harris et al. 2020), PyStructure (J. den Brok et al. 2024), PHANGS–ALMA pipeline (v3.1; A. K. Leroy et al. 2021a).

Appendix A
ALMA Flux Recovery

A main challenge with interferometric ALMA data remains the reliability of the combined 7 m+TP observations and their ability to recover CO emission, accounting for the *u–v* coverage and calibration uncertainties. We note, however, that significant prior work has been devoted to precisely quantify the issue of flux recovery in the context of nearby galaxy CO emission. A. K. Leroy et al. (2021a) investigated the calibration and reliability of ALMA TP observations by comparing these fluxes of the four separate TP antennas, finding rms variations of 2%–4% due to flux calibration uncertainties. Furthermore, A. K. Leroy et al. (2021a) and L. Neumann et al. (2023a) demonstrated that combined 7 m +TP observations reliably recover >90% of the total flux in simulated data sets for nearby face-on galaxies. In Figure 15, we plot the distribution of the ALMA 7 m visibilities (averaged over all channels and time) in terms of *uv*-distance for CO(1–0) and CO(2–1) for one galaxy in our sample (here NGC 0685). When including the ALMA TP observations, the overlap for CO(1–0) and CO(2–1) extends to ∼18 kλ in *uv*-distance, corresponding to an angular resolution of ∼14″.

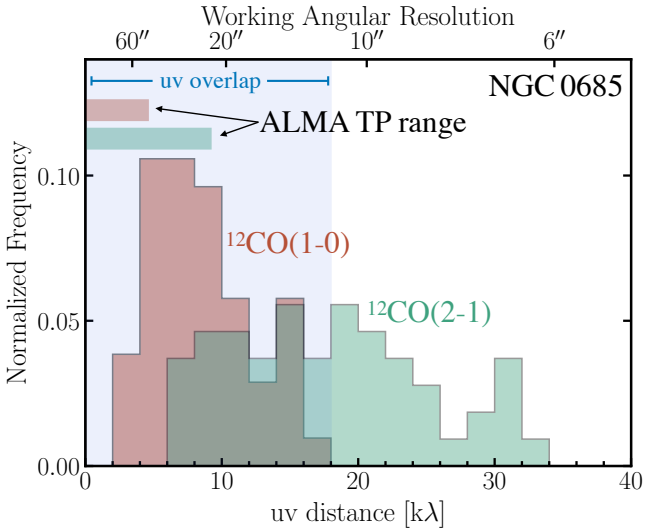

Figure 15. Overlap in *uv*-distance for CO(1–0) and CO(2–1) 7 m+TP observations. The normalized histograms illustrate the distribution of the channel and time-averaged amplitudes of the visibilities for the ALMA 7 m observations of CO(1–0) in brown and CO(2–1) in green. In addition, the range of the TP observations is indicated by the bars. The blue shaded region represents the overlap in terms of *uv*-distance out to ∼18 kλ (∼14″).

Appendix B
Comparing Different R_{21} Fitting Prescriptions

In Section 4.1.2, we use a power-law function to fit the relation between the SFR surface density (Σ_{SFR}) and the line ratio (see Figure 6). However, the underlying relation is likely more complex than a simple, single exponential law, and hence, alternative functional forms have been proposed in previous studies. Critically, however, we are limited to a narrow range of SFR surface density, over which R_{21} scales following an exponential law. For completeness, we provide here a comparison of such alternative prescriptions (see Table 6 for overview). We note however, that given the limited dynamical range in SFR surface density, such parameterization is not clearly justified by the data, as the statistical improvement (in terms of reduced χ^2) is insignificant. Figure 16 illustrates the different prescriptions.

An alternative, physically motivated, scaling relation for the line ratio is proposed by A. K. Leroy et al. (2022; hereafter called broken power law). This functional form adopts a maximum line ratio at 1 and a minimal line ratio at y_{low}. The motivation is that we do not expect the line ratio to exceed, on kiloparsec scales, significantly above unity, and we do not expect the line ratio to decrease arbitrarily low, even at low SFR surface densities. In between, the ratios are described with an exponential power law. When fitting such a broken power law to our data, we find a slightly higher reduced χ^2 of 0.090 (compared to 0.077 using the simple power law). Finally, we can also describe the R_{21} relation using a two-component power-law approach. The two-component

Table 6
Different Functional Forms of the Scaling Relation of the Line Ratio ($y \equiv \log_{10}(R_{21})$) and the SFR Surface Density ($x \equiv \log_{10}(\Sigma_{\rm SFR})$)

Prescription	Functional Form	Reduced χ^2
Simple Power law	$y = m \cdot x + q$	0.077
Broken Power law	$y = \begin{cases} y_{\rm low} & x < x_{\rm low} \\ y_{\rm low} + m \cdot (x - x_{\rm low}) & x_{\rm low} \leqslant x \leqslant x_{\rm high} \\ 0.0 & x > x_{\rm high} \end{cases}$	0.090
Two-component Power law	$y = \begin{cases} m_1 \cdot x + q & x < x_0 \\ m_2 \cdot x + (m_1 - m_2) \cdot x_0 & x \geqslant x_0 \end{cases}$	0.075

Note. The reduced χ^2 is derived from the fit shown in Figure 16.

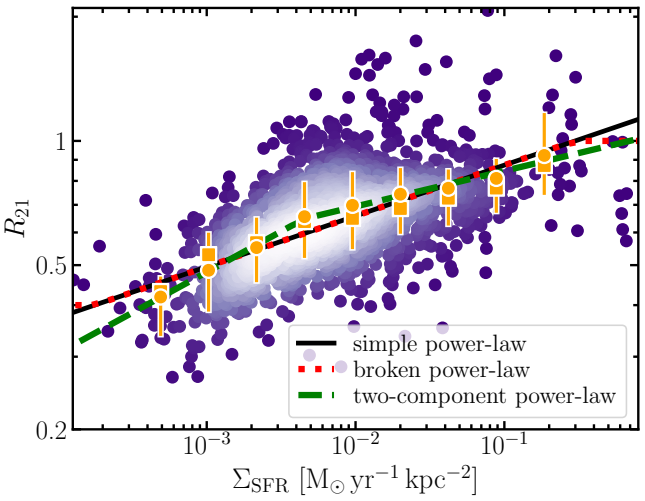

Figure 16. Contrasting different R_{21} fitting prescriptions. In the paper, we employ a simple power law (black line) to describe the scaling relation between the line ratio and the SFR surface density. Alternate functional forms of the scaling relations have been suggested, capturing different, physically motivated aspects. For instance, A. K. Leroy et al. (2022) proposed a broken power law (red dotted line), which described the scaling relation using a power law with a maximum and minimum line ratio. In addition, a two-component power law can also be used, which describes the contribution from a star-forming and non-star-forming H_2 gas component. We list the respective reduced χ^2 values for these functional forms in Table 6.

approach is motivated by separating the gas into an SF-related versus non-SF-related H_2 phase. Calculating the reduced χ^2 value of 0.075, we find that it is only insignificantly better than the simple power law. Therefore, given, in particular, the limitation by the dynamical range that the data cover in terms of SFR surface density, the simple power-law prescription is used.

ORCID iDs

Jakob den Brok https://orcid.org/0000-0002-8760-6157
Elias K. Oakes https://orcid.org/0000-0002-0119-1115
Adam K. Leroy https://orcid.org/0000-0002-2545-1700
Eric W. Koch https://orcid.org/0000-0001-9605-780X
Antonio Usero https://orcid.org/0000-0003-1242-505X
Erik W. Rosolowsky https://orcid.org/0000-0002-5204-2259
Frank Bigiel https://orcid.org/0000-0003-0166-9745
Jiayi Sun (孙嘉懿) https://orcid.org/0000-0003-0378-4667
Hao He https://orcid.org/0000-0001-9020-1858
Ashley T. Barnes https://orcid.org/0000-0003-0410-4504
Yixian Cao https://orcid.org/0000-0001-5301-1326
Fu-Heng Liang https://orcid.org/0000-0003-2496-1247
Hsi-An Pan https://orcid.org/0000-0002-1370-6964
Sumit K. Sarbadhicary https://orcid.org/0000-0002-4781-7291
Thomas G. Williams https://orcid.org/0000-0002-0012-2142

References

Anand, G. S., Lee, J. C., Van Dyk, S. D., et al. 2021, MNRAS, 501, 3621
Astropy Collaboration, Price-Whelan, A. M., Lim, P. L., et al. 2022, ApJ, 935, 167
Astropy Collaboration, Price-Whelan, A. M., Sipőcz, B. M., et al. 2018, AJ, 156, 123
Astropy Collaboration, Robitaille, T. P., Tollerud, E. J., et al. 2013, A&A, 558, A33
Bassini, L., Rasia, E., Borgani, S., et al. 2020, A&A, 642, A37
Belfiore, F., Leroy, A. K., Sun, J., et al. 2023, A&A, 670, A67
Bigiel, F., Leroy, A., Walter, F., et al. 2008, AJ, 136, 2846
Bolatto, A. D., Wolfire, M., & Leroy, A. K. 2013, ARA&A, 51, 207
Braine, J., & Combes, F. 1992, A&A, 264, 433
Braine, J., Combes, F., Casoli, F., et al. 1993, A&AS, 97, 887
Braine, J., Ferguson, A. M. N., Bertoldi, F., & Wilson, C. D. 2007, ApJL, 669, L73
Brown, T., Wilson, C. D., Zabel, N., et al. 2021, ApJS, 257, 21
Bruzual, G., & Charlot, S. 2003, MNRAS, 344, 1000
Bryant, P. M., & Scoville, N. Z. 1996, ApJ, 457, 678
Calzetti, D., Kennicutt, R. C., Engelbracht, C. W., et al. 2007, ApJ, 666, 870
CASA Team, Bean, B., Bhatnagar, S., et al. 2022, PASP, 134, 114501
Casasola, V., Bianchi, S., De Vis, P., et al. 2020, A&A, 633, A100
Chabrier, G. 2003, PASP, 115, 763
Cicone, C., Bothwell, M., Wagg, J., et al. 2017, A&A, 604, A53
Crosthwaite, L. P., & Turner, J. L. 2007, AJ, 134, 1827
den Brok, J., Neumann, L., Eibensteiner, C., et al. 2024, jdenbrok/PyStructure: PyStructure_v3.0.1, Zenodo, doi:10.5281/zenodo.13787728
den Brok, J. S., Bigiel, F., Chastenet, J., et al. 2023a, A&A, 676, A93
den Brok, J. S., Chatzigiannakis, D., Bigiel, F., et al. 2021, MNRAS, 504, 3221
den Brok, J. S., Leroy, A. K., Usero, A., et al. 2023b, MNRAS, 526, 6347
Dickman, R. L., Snell, R. L., & Schloerb, F. P. 1986, ApJ, 309, 326
Eckart, A., Downes, D., Genzel, R., et al. 1990, ApJ, 348, 434
Eibensteiner, C., Barnes, A. T., Bigiel, F., et al. 2022, A&A, 659, A173
Emsellem, E., Schinnerer, E., Santoro, F., et al. 2022, A&A, 659, A191
Fazio, G. G., Hora, J. L., Allen, L. E., et al. 2004, ApJS, 154, 10
Francis, L., Johnstone, D., Herczeg, G., Hunter, T. R., & Harsono, D. 2020, AJ, 160, 270
Gallagher, M. J., Leroy, A. K., Bigiel, F., et al. 2018, ApJ, 858, 90
Gong, M., Ostriker, E. C., Kim, C.-G., & Kim, J.-G. 2020, ApJ, 903, 142
Goulding, A. D., & Alexander, D. M. 2009, MNRAS, 398, 1165
Groves, B., Kreckel, K., Santoro, F., et al. 2023, MNRAS, 520, 4902
Harris, C. R., Millman, K. J., van der Walt, S. J., et al. 2020, Natur, 585, 357
Hasegawa, T., Morino, J., Sorai, K., et al. 1997, in ASP Conf. Ser. 124, Diffuse Infrared Radiation and the IRTS, ed. H. Okuda, T. Matsumoto, & T. Rollig (San Francisco, CA: ASP), 244
Heyer, M., & Dame, T. M. 2015, ARA&A, 53, 583
Hu, C.-Y., Sternberg, A., & van Dishoeck, E. F. 2023, ApJ, 952, 140
Hunter, T. R., Indebetouw, R., Brogan, C. L., et al. 2023, PASP, 135, 074501
Keating, L. C., Richings, A. J., Murray, N., et al. 2020, MNRAS, 499, 837
Keenan, R. P., Marrone, D. P., & Keating, G. K. 2025, ApJ, 979, 228
Keenan, R. P., Marrone, D. P., Keating, G. K., et al. 2024, ApJ, 975, 150

Kennicutt, R. C., Jr. 1998, ARA&A, 36, 189
Kennicutt, R. C., Jr., & Evans, N. J. 2012, ARA&A, 50, 531
Kepley, A. A., Leroy, A. K., Johnson, K. E., Sandstrom, K., & Chen, C. H. R. 2016, ApJ, 828, 50
Koda, J., Hirota, A., Egusa, F., et al. 2023, ApJ, 949, 108
Koda, J., Sawada, T., Sakamoto, K., et al. 2020, ApJL, 890, L10
Koda, J., Scoville, N., Hasegawa, T., et al. 2012, ApJ, 761, 41
Lamperti, I., Saintonge, A., Koss, M., et al. 2020, ApJ, 889, 103
Lang, P., Meidt, S. E., Rosolowsky, E., et al. 2020, ApJ, 897, 122
Law, C. J., Zhang, Q., Ricci, L., et al. 2018, ApJ, 865, 17
Lee, H., Skillman, E. D., Cannon, J. M., et al. 2006, ApJ, 647, 970
Lequeux, J., Le Bourlot, J., Pineau des Forets, G., et al. 1994, A&A, 292, 371
Leroy, A. K., Bolatto, A., Gordon, K., et al. 2011, ApJ, 737, 12
Leroy, A. K., Hughes, A., Liu, D., et al. 2021a, ApJS, 255, 19
Leroy, A. K., Rosolowsky, E., Usero, A., et al. 2022, ApJ, 927, 149
Leroy, A. K., Sandstrom, K. M., Lang, D., et al. 2019, ApJS, 244, 24
Leroy, A. K., Schinnerer, E., Hughes, A., et al. 2021b, ApJS, 257, 43
Leroy, A. K., Usero, A., Schruba, A., et al. 2017, ApJ, 835, 217
Leroy, A. K., Walter, F., Bigiel, F., et al. 2009, AJ, 137, 4670
Leroy, A. K., Walter, F., Brinks, E., et al. 2008, AJ, 136, 2782
Leroy, A. K., Walter, F., Sandstrom, K., et al. 2013, AJ, 146, 19
Liu, D., Schinnerer, E., Saito, T., et al. 2023, A&A, 672, A36
Narayanan, D., & Krumholz, M. R. 2014, MNRAS, 442, 1411
Neumann, L., den Brok, J. S., Bigiel, F., et al. 2023a, A&A, 675, A104
Neumann, L., Gallagher, M. J., Bigiel, F., et al. 2023b, MNRAS, 521, 3348
Papadopoulos, P. P., & Seaquist, E. R. 1998, ApJ, 492, 521
Peñaloza, C. H., Clark, P. C., Glover, S. C. O., Shetty, R., & Klessen, R. S. 2017, MNRAS, 465, 2277
Pilyugin, L. S., & Grebel, E. K. 2016, MNRAS, 457, 3678
Remijan, A., Biggs, A., Cortes, P. A., et al. 2019, ALMA Technical Handbook, ALMA Doc. 7.3, ver. 1.1, Zenodo, doi:10.5281/zenodo.4511522
Saintonge, A., & Catinella, B. 2022, ARA&A, 60, 319
Saintonge, A., Catinella, B., Tacconi, L. J., et al. 2017, ApJS, 233, 22
Sakamoto, S., Hayashi, M., Hasegawa, T., Handa, T., & Oka, T. 1994, ApJ, 425, 641
Salim, S., Boquien, M., & Lee, J. C. 2018, ApJ, 859, 11
Salim, S., Lee, J. C., Janowiecki, S., et al. 2016, ApJS, 227, 2
Sandstrom, K. M., Leroy, A. K., Walter, F., et al. 2013, ApJ, 777, 5
Sawada, T., Hasegawa, T., Handa, T., et al. 2001, ApJS, 136, 189
Schinnerer, E., & Leroy, A. K. 2024, ARA&A, 62, 369
Schmidt, M. 1959, ApJ, 129, 243
Schmitt, H. R., Calzetti, D., Armus, L., et al. 2006, ApJS, 164, 52
Schruba, A., Leroy, A. K., Walter, F., et al. 2011, AJ, 142, 37
Seifried, D., Haid, S., Walch, S., Borchert, E. M. A., & Bisbas, T. G. 2020, MNRAS, 492, 1465
Sheth, K., Regan, M., Hinz, J. L., et al. 2010, PASP, 122, 1397
Shirley, Y. L. 2015, PASP, 127, 299
Solomon, P. M., Rivolo, A. R., Barrett, J., & Yahil, A. 1987, ApJ, 319, 730
Solomon, P. M., & Vanden Bout, P. A. 2005, ARA&A, 43, 677
Sun, J., Leroy, A. K., Ostriker, E. C., et al. 2023, ApJL, 945, L19
Sun, J., Leroy, A. K., Rosolowsky, E., et al. 2022, AJ, 164, 43
Teng, Y.-H., Sandstrom, K. M., Sun, J., et al. 2023, ApJ, 950, 119
Tremonti, C. A., Heckman, T. M., Kauffmann, G., et al. 2004, ApJ, 613, 898
Usero, A., Leroy, A. K., Walter, F., et al. 2015, AJ, 150, 115
Villanueva, V., Bolatto, A. D., Vogel, S. N., et al. 2024, ApJ, 962, 88
Williams, T. G., Kreckel, K., Belfiore, F., et al. 2022, MNRAS, 509, 1303
Wong, T., & Blitz, L. 2002, ApJ, 569, 157
Yajima, Y., Sorai, K., Miyamoto, Y., et al. 2021, PASJ, 73, 257
Yoda, T., Handa, T., Kohno, K., et al. 2010, PASJ, 62, 1277
Young, J. S., Allen, L., Kenney, J. D. P., Lesser, A., & Rownd, B. 1996, AJ, 112, 1903
Young, J. S., & Scoville, N. Z. 1991, ARA&A, 29, 581
Young, J. S., Xie, S., Tacconi, L., et al. 1995, ApJS, 98, 219